Letter of Intent
for

Antiproton–Proton Scattering Experiments with Polarization

(PAX Collaboration)

Jülich, January 15, 2003

Letter of Intent
for

Antiproton–Proton Scattering Experiments with Polarization

(PAX Collaboration)

Abstract

Polarized antiprotons produced by spin filtering with an internal polarized gas target provide access to a wealth of single– and double–spin observables, thereby opening a window to physics uniquely accessible at the HESR. This includes a first measurement of the transversity distribution of the valence quarks in the proton, a test of the predicted opposite sign of the Sivers–function, related to the quark distribution inside a transversely polarized nucleon, in Drell–Yan (DY) as compared to semi–inclusive DIS, and a first measurement of the moduli and the relative phase of the time–like electric and magnetic form factors $G_{E,M}$ of the proton. In polarized and unpolarized $p\bar{p}$ elastic scattering open questions like the contribution from the odd charge–symmetry Landshoff–mechanism at large $|t|$ and spin–effects in the extraction of the forward scattering amplitude at low $|t|$ can be addressed. The proposed detector consists of a forward dipole spectrometer with excellent particle identification and a non–magnetic large–angle apparatus optimized for the detection of DY electron pairs.

Members of the Collaboration

Beijing, P.R. China, Department of Physics

Bo–Qiang Ma

Bochum, Germany, Institut für Theoretische Physik II, Ruhr Universität Bochum

Klaus Goeke, Andreas Metz, and Peter Schweitzer

Bonn, Germany, Helmholtz–Institut für Strahlen– und Kernphysik

Jens Bisplinghoff, Paul–Dieter Eversheim, Frank Hinterberger, Ulf–G. Meißner, and Heiko Rohdjeß

Dubna, Russia, Laboratory of Nuclear Problems, Joint Institute for Nuclear Research

Sergey Dymov, Natela Kadagidze, Vladimir Komarov, Anatoly Kulikov, Vladimir Kurbatov, Vladimir Leontiev, Gogi Macharashvili, Sergey Merzliakov, Valerie Serdjuk, Sergey Trusov, Yuri Uzikov, Alexander Volkov, and Nikolai Zhuravlev

Dubna, Russia, Laboratory of Particle Physics, Joint Institute for Nuclear Research

Igor Savin, Vasily Krivokhizhin, Alexander Nagaytsev, Gennady Yarygin, Gleb Meshcheryakov, Binur Shaikhatdenov, Oleg Ivanov, Oleg Shevchenko, and Vladimir Peshekhonov

Erlangen, Germany, Physikalisches Institut, Universität Erlangen–Nürnberg

Wolfgang Eyrich, Andro Kacharava, Bernhard Krauss, Albert Lehmann, David Reggiani, Klaus Rith, Ralf Seidel, Erhard Steffens, Friedrich Stinzing, Phil Tait, and Sergey Yaschenko

Ferrara, Italy, Instituto Nationale di Fisica Nucleare

Guiseppe Ciullo, Marco Contalbrigo, Marco Capiluppi, Paola Ferretti–Dalpiaz, Alessandro Drago, Paolo Lenisa, Michelle Stancari, and Marco Statera

Frascati, Italy, Instituto Nationale di Fisica Nucleare

Nicola Bianchi, Enzo De Sanctis, Pasquale Di Nezza, Delia Hasch, Valeria Muccifora, Karapet Oganessyan, and Patrizia Rossi

Gatchina, Russia, Petersburg Nuclear Physics Institute

Stanislav Belostotski, Oleg Grebenyuk, Kirill Grigoriev, Peter Kravtsov, Anton Izotov, Anton Jgoun, Sergey Manaenkov, Maxim Mikirtytchiants, Oleg Miklukho, Yuriy Naryshkin, Alexandre Vassiliev, and Andrey Zhdanov

Gent, Belgium, Department of Subatomic and Radiation Physics, University of Gent

Dirk Ryckbosch

Jülich, Germany, Forschungszentrum Jülich, Institut für Kernphysik

David Chiladze, Ralf Engels, Olaf Felden, Johann Haidenbauer, Christoph Hanhart, Andreas Lehrach, Bernd Lorentz, Nikolai Nikolaev, Siegfried Krewald, Sig Martin, Dieter Prasuhn, Frank Rathmann, Hellmut Seyfarth, Alexander Sibirtsev, and Hans Ströher

Moscow, Russia, Institute for Theoretical and Experimental Physics

Ashot Gasparyan, Vera Grishina, and Leonid Kondratyuk

Moscow, Russia, Lebedev Physical Institute

Alexandre Bagoulia, Evgeny Devitsin, Valentin Kozlov, Adel Terkulov, and Mikhail Zavertiaev

Protvino, Russia, High Energy Physics Institute

N.I. Belikov, B.V. Chuyko, Yu.V. Kharlov, V.A. Korotkov, V.A. Medvedev, A.I. Mysnik, A.F. Prudkoglyad, P.A. Semenov, S.M. Troshin, and M.N. Ukhanov

Tbilisi, Georgia, High Energy Physics Institute, Tbilisi State University

Mikheil Nioradze, and Mirian Tabidze

Torino, Italy, Dipartimento di Fisica Teorica, Universita di Torino and INFN

Mauro Anselmino, Vincenzo Barone, Mariaelena Boglione, and Alexei Prokudin

Yerevan, Armenia, Yerevan Physics Institute

Norayr Akopov, R. Avagyan, A. Avetisyan, S. Taroian, G. Elbakyan, H. Marukyan, and Z. Hakopov

Spokespersons:

Frank Rathmann, E–Mail: f.rathmann@fz–juelich.de
Paolo Lenisa, E–Mail: lenisa@mail.desy.de

Contents

1 Physics Case

1.1 Preface

The polarized antiproton–proton interactions at HESR will give a unique access to a number of new fundamental physics observables, which can be studied neither at other facilities nor at HESR without transverse polarization of protons and/or antiprotons:

- The transversity distribution is the last leading–twist missing piece of the QCD description of the partonic structure of the nucleon. It describes the quark transverse polarization inside a transversely polarized proton [1]. Unlike the more conventional unpolarized quark distribution $q(x, Q^2)$ and the helicity distribution $\Delta q(x, Q^2)$, the transversity $h_1^q(x, Q^2)$ can neither be accessed in deep–inelastic scattering of leptons off nucleons nor can it be reconstructed from the knowledge of $q(x, Q^2)$ and $\Delta q(x, Q^2)$. It may contribute to some single–spin observables, but always coupled to other unknown functions. The transversity distribution is directly accessible uniquely via the **double transverse spin asymmetry** A_{TT} in the Drell–Yan production of lepton pairs. The theoretical expectations for A_{TT} in the Drell–Yan process with transversely polarized antiprotons interacting with a transversely polarized proton target at HESR are in the 30–40 per cent range [2, 3]; with the expected antiproton spin–filtering rate and luminosity of HESR the PAX experiment is uniquely suited for the definitive observation of $h_1^q(x, Q^2)$ of the proton for the valence quarks. The determination of $h_1^q(x, Q^2)$ will open new pathways to the QCD interpretation of single–spin asymmetry (SSA) measurements. In conjunction with the data on SSA from the HERMES collaboration [4], the PAX measurements of the SSA in Drell–Yan production on polarized protons can for the first time provide a test of the theoretical prediction [5] of the reversal of the sign of the Sivers function [6] from semi–inclusive DIS to Drell–Yan production.

- The origin of the unexpected Q^2–dependence of the ratio of the magnetic and electric form factors of the proton as observed at the Jefferson laboratory [7] can be clarified by a measurement of their relative phase in the time–like region, which discriminates strongly between the models for the form factor. This phase can only be measured via SSA in the annihilation $\bar{p}p^\uparrow \to e^+e^-$ on a transversely polarized target [8, 9]. The first ever measurement of this phase at PAX will also contribute to the understanding of the onset of the pQCD asymptotics in the time–like region and will serve as a stringent test of dispersion theory approaches to the relationship between the space–like and time–like form factors [10, 11, 12]. The double–spin asymmetry will allow independently the $G_E - G_M$ separation and serve as a check of the Rosenbluth separation in the time–like region which has not been carried out so far.

- Arguably, in $p\bar{p}$ elastic scattering the hard scattering mechanism can be checked beyond $|t| = \frac{1}{2}(s - 4m_p^2)$ accessible in the t–u–symmetric pp scattering, because in the

$p\bar{p}$ case the u–channel exchange contribution can only originate from the strongly suppressed exotic dibaryon exchange. Consequently, in the $p\bar{p}$ case the hard mechanisms [13, 14, 15] can be tested at t almost twice as large as in pp scattering. Even unpolarized large angle $p\bar{p}$ scattering data can shed light on the origin of the intriguing oscillations around the s^{-10} behavior of the 90^0 scattering in the pp channel and put stringent constraints on the much disputed odd–charge conjugation Landshoff mechanism [16, 17, 18]. If the Landshoff mechanism is suppressed then the double transverse asymmetry in $p\bar{p}$ scattering is expected to be as large as the one observed in the pp case.

- The charge conjugation property allows direct monitoring of the polarization of antiprotons in HESR and the rate of polarization buildup constitutes a direct measurement of the transverse double spin asymmetry in the $p\bar{p}$ total cross section. This asymmetry has never been measured and its knowledge is crucial for the correct extraction of the real part of the forward $p\bar{p}$ scattering amplitude from Coulomb–nuclear interference. The PAX results on the asymmetry will help to clarify the origin of the discrepancy between the dispersion theory calculations [19] and the experimental extraction [20] of the value of the real part of the forward scattering amplitude usually made assuming the spin independence of forward scattering.

1.2 Accessing Transversity Distributions

Spin observables and transversity

There are three leading–twist quantities necessary to achieve a full understanding of the nucleon quark structure: the unpolarized quark distribution $q(x, Q^2)$, the helicity distribution $\Delta q(x, Q^2)$ and the transversity distribution $\Delta_T q(x, Q^2)$ [more usually denoted as $h_1^q(x, Q^2)$] [1]. While Δq describes the quark longitudinal polarization inside a longitudinally polarized proton, the transversity describes the quark transverse polarization inside a transversely polarized proton at infinite momentum. In the non–relativistic limit spin and momentum decouple, leading to $h_1^q = \Delta q$. However, in general these are two independent quantities; moreover, the quark transverse polarization does not mix with the gluon polarization (gluons carry only longitudinal spin), and thus the QCD evolutions of h_1^q and Δq are different. One cannot claim to understand the spin structure of the nucleon until all three leading–twist structure functions have been measured.

Whereas the unpolarized distributions are well known, and more and more information is becoming available on Δq, nothing is known experimentally on the nucleon transversity distribution. From the theoretical side, there exist only a few theoretical models for h_1^q. An upper bound on its magnitude has been derived: this bound holds in the naive parton model, and, if true in QCD at some scale, it is preserved by QCD evolution. Therefore, its verification or disproof would be by itself a very interesting result. The reason why h_1^q, despite its fundamental importance, has never been measured is that it is a chiral–odd function, and consequently it decouples from inclusive deep–inelastic scattering. Since electroweak and strong interactions conserve chirality, h_1^q cannot occur alone, but has to be coupled to a second chiral–odd quantity.

This is possible in polarized Drell–Yan processes, where one measures the product of two transversity distributions, and in semi–inclusive Deep Inelastic Scattering (SIDIS), where one couples h_1^q to a new unknown fragmentation function, the so–called Collins function [21]. Similarly, one could couple h_1^q and the Collins function in transverse single–spin asymmetries (SSA) in inclusive processes like $p^\uparrow p \to \pi X$.

Both HERMES and COMPASS experiments are now gathering data on spin asymmetries in SIDIS processes, which should yield information on some combination of h_1^q and the Collins function. However one can not directly extract an information on h_1^q alone: the measured spin asymmetries can originate also from the Sivers function [6] – a spin property of quark distributions, rather than fragmentation – which does not couple to transversity; in addition, higher twist effects might still be sizeable at the modest Q^2 of the two experiments, thus making the interpretation of data less clear. The transverse SSA experimentally observed in $p^\uparrow p \to \pi X$ and $\bar{p}^\uparrow p \to \pi X$ processes [22, 23, 24] can be interpreted in terms of transversity and Collins functions; however, also here contributions from the Sivers function are important and these processes could hardly be used to extract information on h_1^q alone.

Transversity in Drell–Yan processes at PAX

The most direct way to obtain information on transversity – the last leading–twist missing piece of the nucleon spin structure – is the measurement of the double transverse spin asymmetry A_{TT} in Drell–Yan processes with *both transversely polarized beam and target*:

$$A_{TT} \equiv \frac{d\sigma^{\uparrow\uparrow} - d\sigma^{\uparrow\downarrow}}{d\sigma^{\uparrow\uparrow} + d\sigma^{\uparrow\downarrow}} = \hat{a}_{TT} \, \frac{\sum_q e_q^2 \, h_1^q(x_1, M^2) \, h_1^{\bar{q}}(x_2, M^2)}{\sum_q e_q^2 \, q(x_1, M^2) \, \bar{q}(x_2, M^2)} \,, \tag{1}$$

where $q = u, \bar{u}, d, \bar{d}, ...$, M is the invariant mass of the lepton pair and $\hat{a}_{TT}$ is the double spin asymmetry of the QED elementary process, $q\bar{q} \to \ell^+\ell^-$,

$$\hat{a}_{TT} = \frac{\sin^2\theta}{1 + \cos^2\theta} \, \cos 2\phi \,, \tag{2}$$

with θ the polar angle of the lepton in the l^+l^- rest frame and ϕ the azimuthal angle with respect to the proton polarization.

The measurement of A_{TT} is planned at RHIC, in Drell–Yan processes with transversely polarized protons. In this case one measures the product of two transversity distributions, one for a quark and one for an antiquark (both in a proton). At RHIC energies one expects measurements at $\tau = x_1 x_2 = M^2/s \simeq 10^{-3}$, which mainly leads to the exploration of the sea quark proton content, where polarization is likely to be tiny. Moreover, the QCD evolution of transversity is such that, in the kinematical regions of RHIC data, $h_1^q(x, Q^2)$ is much smaller than the corresponding values of $\Delta q(x, Q^2)$ and $q(x, Q^2)$. All this makes the double spin asymmetry A_{TT} expected at RHIC very small, of the order of a per cent or less [25].

The situation with the PAX measurement of the double transverse spin asymmetry A_{TT} in Drell–Yan processes with *polarized antiprotons and protons*, $\bar{p}^{\uparrow} p^{\uparrow} \to \ell^+\ell^- X$, is a much more favorable one. The expected PAX values of $s \simeq 30$–50 GeV^2 and $M^2 \simeq 10$ GeV^2 are well suited for the definitive observation of A_{TT}. There are some unique features which strongly suggest to pursue the study of h_1^q in the $\bar{p}p$ channel with PAX:

- In $\bar{p}p$ processes both the quark (from the proton) and antiquark (from the antiproton) contributions are large. For typical PAX kinematics one has $\tau = x_1 x_2 = M^2/s \simeq 0.2$ – 0.3, which means that only quarks and antiquarks with large x contribute, that is valence quarks for which h_1^q is expected to be large. Moreover, at such x and M^2 values the QCD evolution does not suppress $h_1^q(x, Q^2)$. $A_{TT}/\hat{a}_{TT}$ is expected to be as large as 30% [2]; this is confirmed by direct calculations using the available models for transversity distributions, some of which predict even larger values, up to 40–45% [3]. Actually, all these models agree in having $|h_1^u| \gg |h_1^d|$ [1], so that Eq. (1) for $\bar{p}p$ processes at PAX essentially becomes,

  $$A_{TT} \simeq \hat{a}_{TT} \, \frac{h_1^u(x_1, M^2)\, h_1^u(x_2, M^2)}{u(x_1, M^2)\, u(x_2, M^2)} \,, \tag{3}$$

  where all distribution functions refer to protons ($\bar{q}^{\bar{p}} = q^p = q$, *etc.*).

  An example of a prediction of the asymmetry $A_{TT}/\hat{a}_{TT}$ as a function of $x_{\rm F} = x_1 - x_2$ at $M^2 = 16$ GeV^2 is shown in Fig. 1, indicating that the expected asymmetry is about 0.3 [2]. Similar results are found at smaller values of M^2. The measurement of a large A_{TT} and the determination of the valence quark dominated h_1^q at PAX is distinct from the possible measurement of a very small asymmetry at RHIC which would probe the very different sea quark region. Furthermore, the Drell–Yan events at HESR will get their main contribution from the $x_1 \simeq x_2 \simeq \sqrt{\tau}$ region, so that from the PAX data alone one can essentially access and deduce the x–dependence of $h_1^u(x, M^2)$, which is important for any further applications of the so determined $h_1^u(x, M^2)$ to the interpretation of the SSA measurements.

- Regarding the counting rates, we notice that in the quest for h_1^q one should not confine to the $M > 4$ GeV region, which is usually considered as the "safe" region for the comparison with the pQCD computations, as this cut–off eliminates the background from the $J/\Psi, \Psi'$ production and their subsequent leptonic decay. The contribution to the total cross section from the $J/\Psi, \Psi'$ resonance region in which the cross section increases by almost 2 orders of magnitude going from $M = 4$ to $M = 3$ GeV [26, 27], involves unknown quantities related to the $q\bar{q} - J/\Psi$ coupling. However, independently of these unknown quantities, the $q\bar{q} - J/\Psi$ coupling is a vector one, with the same spinor and Lorentz structure as the $q\bar{q} - \gamma^*$ coupling; similarly for the $J/\Psi - e^+e^-$ decay. These unknown quantities cancel in the ratio giving A_{TT}, while the helicity structure remains, so that Eq. (3) still holds in the J/Ψ resonance region [2]. This possibility of using the Drell–Yan continuum expression at $M < 4$ GeV in the $J/\Psi, \Psi'$ resonance region, in conjunction with the resonance data, enhances substantially the sensitivity of the PAX experiment to A_{TT} and to obtaining direct information on $h_1^u(x_1, M^2)\, h_1^u(x_2, M^2)$.

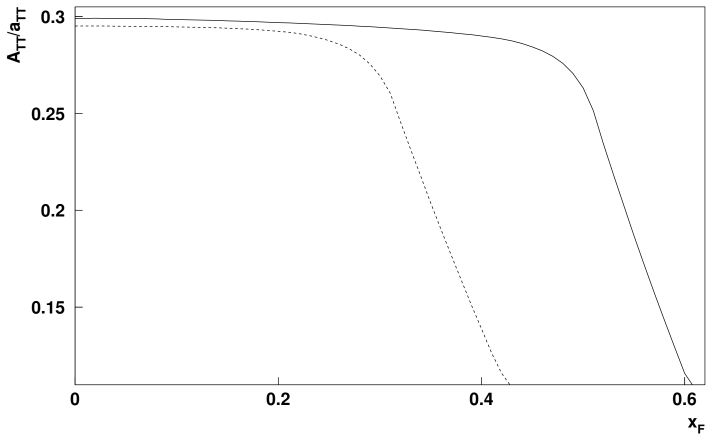

Figure 1: Calculated asymmetry $A_{TT}/\hat{a}_{TT}$ [Eq. (3)] in $\bar{p}p$ Drell–Yan production as a function of $x_{\rm F}$ at $M^2 = 16$ GeV^2 [2]. The solid line corresponds to a beam energy of $T = 22$ GeV, the dashed line is for $T = 15$ GeV.

The double transverse spin asymmetry A_{TT} can be studied also for other processes; in particular, the open charm production, $\bar{p}^\uparrow\, p^\uparrow \to D\, X$ allows one to access transversity distributions. The large x_F production of D mesons is dominated by the $\bar{q}q \to \bar{c}c$ elementary process; then one has (again, all distribution functions refer to protons):

$$A_{TT}^{D} \simeq \frac{\sum_q h_1^q(x_1) \otimes h_1^q(x_2) \otimes \Delta\hat{\sigma} \otimes D(z)}{\sum_q q(x_1) \otimes q(x_2) \otimes \hat{\sigma} \otimes D}\,, \tag{4}$$

which supplies information about the convolution of transversity distributions with the fragmentation functions $D(z)$ of c quarks or antiquarks into D mesons; $\Delta\hat{\sigma} = \hat{\sigma}^{\uparrow\uparrow} - \hat{\sigma}^{\uparrow\downarrow}$, related to the $\bar{q}q \to \bar{c}c$ elementary process. Eq. (4) holds above the resonance region ($M = \sqrt{x_1 x_2 s} > 4$ GeV); the elementary interaction is a pQCD process, so that the cross section for D–production might even be larger, at the same values of M, than the corresponding one for Drell–Yan processes.

Single Spin Asymmetries

While the direct access to transversity is the outstanding, unique possibility offered by the PAX proposal concerning the proton spin structure, there are several other spin observables which should not be forgotten; these might be measurable even before the antiproton polarization is achieved.

The perturbative QCD spin dynamics, with the helicity conserving quark–gluon couplings, is very simple. However, such a simplicity does not always show in the hadronic spin observables; the non–perturbative, long–distance QCD physics has many spin properties, yet to be explored. For example, subtle spin effects related to parton intrinsic motion in distribution functions and in fragmentation processes have been proposed and might be responsible for observed single spin asymmetries; a QCD single spin phenomenology seems to be possible, but more data and new measurements are crucially needed.

A typical example of such an aspect of QCD is supplied by the transverse Single Spin Asymmetries (SSA),

$$A_N = \frac{d\sigma^{\uparrow} - d\sigma^{\downarrow}}{d\sigma^{\uparrow} + d\sigma^{\downarrow}} ,$$

measured in $p^{\uparrow}\, p \to \pi\, X$ and $\bar{p}^{\uparrow}\, p \to \pi\, X$ processes: the SSA at large values of x_F ($x_F \gtrsim 0.4$) and moderate values of p_T ($0.7 < p_T < 2.0$ GeV/c) have been found by several experiments [22, 23, 24] to be unexpectedly large. These asymmetries have clear features:

- pion production at large x_F values originates from valence quarks, and indeed the sign of A_N (positive for π^+, π^0 and negative for π^-) reflects the expected sign of u and d quark polarization;
- similar values and trends of A_N have been found in experiments with center of mass energies ranging from 6.6 up to 200 GeV: this seems to hint at an origin of A_N related to fundamental properties of quark distribution and/or fragmentation.

A new experiment with antiprotons scattered off a polarized proton target, in a new kinematical region, could certainly add information on such spin properties of QCD.

Recently, several papers have stressed the importance of measuring SSA in Drell–Yan processes [28, 29, 30, 31, 32]; these measurements allow the determination of new non–perturbative spin properties of the proton, like the Sivers function, which gives the distribution of quarks in a transversely polarized proton [6]. The SSA are typically generated by so–called time–reversal odd (T–odd) correlation functions. Recently, it became clear that measuring SSA in Drell–Yan processes (like $\bar{p}\, p^{\uparrow} \to l^+\, l^-\, X$ or $\bar{p}^{\uparrow}\, p \to l^+\, l^-\, X$) would check crucially our present day understanding of the mechanism leading to non–vanishing T–odd correlation functions [32, 33]. Non–zero T–odd parton distributions (like the Sivers function $f_{1T}^{\perp}$) can be obtained only if the path–ordered exponential in the operator definition, which ensures color gauge invariance and encodes initial state interactions (in Drell–Yan) or final state interactions of the struck quark (in SIDIS), is taken into account. This picture of the underlying mechanism of non–zero T–odd effects leads to the very interesting prediction, that in Drell–Yan and in semi–inclusive DIS T–odd functions should have a reversed sign [5], which in particular implies that

$$f_{1T}^{\perp}\Big|_{DY} = -f_{1T}^{\perp}\Big|_{DIS} . \tag{5}$$

In the meantime, the HERMES collaboration has obtained the first preliminary result for the Sivers asymmetry (of about 10%) in semi–inclusive DIS. This allows one to check the predicted sign–flip in the valence region via the corresponding Drell–Yan measurement of the Sivers function at PAX. Such a study would be extremely interesting and important even if the error bars would be large.

In general, combining information on SSA from $p\,p^\uparrow$ and $\bar{p}^\uparrow\,p$ processes would not only greatly help in disentangling the Sivers and Collins contribution, and thus offering a better access to h_1^q from SSA data, but would also allow one to check our current understanding of the origin of SSA in QCD in an unprecedented way.

1.3 Electromagnetic Form Factors of the Proton

The form factors of hadrons as measured in both the space–like and time–like domains provide fundamental information on the structure and internal dynamics of hadrons. Both the analytic structure and phases of the form factors in the time–like regime are connected by dispersion relations (DR) to the space–like regime [10, 11, 12, 34, 35]. The recent experiments raised two serious issues: first, the Fermilab E835 measurements of $|G_M(q^2)|$ of the proton at $q^2 = 11.63$ and 12.43 GeV^2 ([36] and references therein) have shown that $|G_M(q^2)|$ in the time–like region is twice as large as in the space–like region (there are some uncertainties because the direct $G_E - G_M$ separation was not possible due to statistics and acceptance); second, the studies of the electron–to–proton polarization transfer in $\overrightarrow{e}^-\,p \to e^-\,\overrightarrow{p}$ scattering at Jefferson Laboratory [7] show that the ratio of Sachs form factors $G_E(q^2)/G_M(q^2)$ is monotonically decreasing with increasing $Q^2 = -q^2$, in strong contradiction with the G_E/G_M scaling assumed in the traditional Rosenbluth separation method, which may in fact not be reliable in the space–like region.

Although the space–like form factors of a stable hadron are real, the time–like form factors have a phase structure reflecting the final–state interactions (FSI) of the outgoing hadrons. Kaidalov et al. argue that the same FSI effects are responsible for the enhancement of $|G_M(q^2)|$ in the time–like region [37]; their evaluation of the enhancement based on the variation of Sudakov effects from the space–like to time–like region is consistent with general requirements from analyticity that FSI effects vanish at large q^2 in the pQCD asymptotics, the recent discussion is found in Brodsky et al. ([9], see also [12]). The same property is shared by the hybrid pQCD–DR description developed by Hammer, Meissner and Drechsel [11].

Brodsky et al. make a strong point that the new Jefferson Laboratory results make it critical to carefully identify and separate the time–like G_E and G_M form factors by measuring the center–of–mass angular distribution and the polarization of the proton in $e^+e^- \to p\bar{p}$ or the transverse SSA in polarized $p^\uparrow\bar{p} \to \ell^+\ell^-$ reactions [9]. As noted by Dubnickova, Dubnicka, and Rekalo [8] and by Rock [38], the nonzero phase difference between G_E and G_M form factors entails the normal polarization $\mathcal{P}_y$ of the final state (anti)baryons in $e^-e^+ \to \overrightarrow{p}\bar{p}$ or the transverse SSA $\mathcal{A}_y = \mathcal{P}_y$ in annihilation $p^\uparrow\bar{p} \to e^-e^+$ on transversely polarized protons:

$$\mathcal{A}_y = \frac{\sin 2\theta\,\mathrm{Im}G_E^* G_M}{[(1+\cos^2\theta)|G_M|^2 + \sin^2\theta|G_E|^2/\tau]\sqrt{\tau}} \tag{6}$$

where $\tau \equiv q^2/4m_p^2 > 1$ and θ is the scattering angle.

As emphasized already by Dubnickova et al. the knowledge of the phase difference between the G_E and G_M may strongly constrain the models for the form factors. More recently there have been a number of explanations and theoretically motivated fits of the new data on the proton F_2/F_1 data [39, 40, 41, 42]. Each of the models predict a specific fall–off and phase structure of the form factors from $s \leftrightarrow t$ crossing to the time–like domain. The predicted single–spin asymmetry is substantial and has a distinct q^2 dependence which strongly discriminates between the analytic forms which fit the proton G_E/G_M data in the space–like region. This is illustrated clearly in Fig. 2.

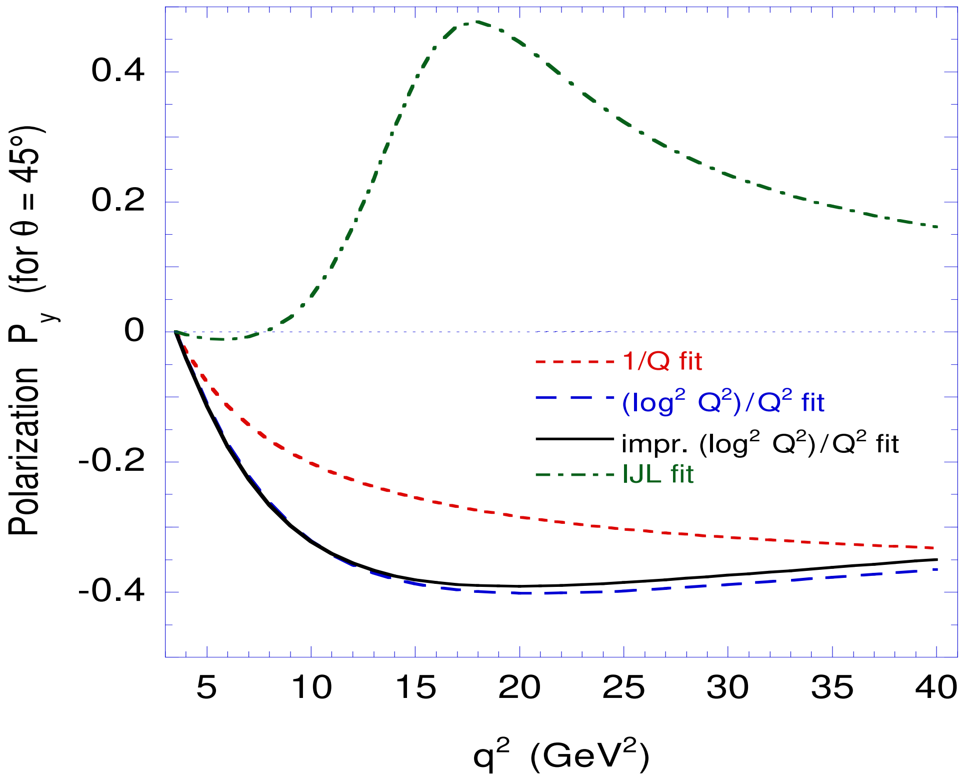

Figure 2: Predicted single–spin asymmetry $\mathcal{A}_y = \mathcal{P}_y$ for $\theta = 45°$ in the time–like region for selected form factor fits: $F_2/F_1 \propto 1/Q$ fit [9], the $(\log^2 Q^2)/Q^2$ fit of Belitsky *et al.* [39]; an improved $(\log^2 Q^2)/Q^2$ fit [42]; and a fit from Iachello *et al.*, [43].

Despite the fundamental implications of the phase for an understanding of the connection between the space–like and time–like form factors, such measurements have never been made. The available data on $|G_M^{(p)}|$ in the time–like region are scarce, as can be seen from Fig. 3.

However, these data suggest the existence of additional structures in the time–like form factor of the proton; as Hammer, Meissner and Drechsel emphasized [11] that calls for improvements in the dispersion–theoretical description of form factors. At larger q^2 the data from E835 [44, 36] and E760 [45] seem to approach the power–law behavior predicted

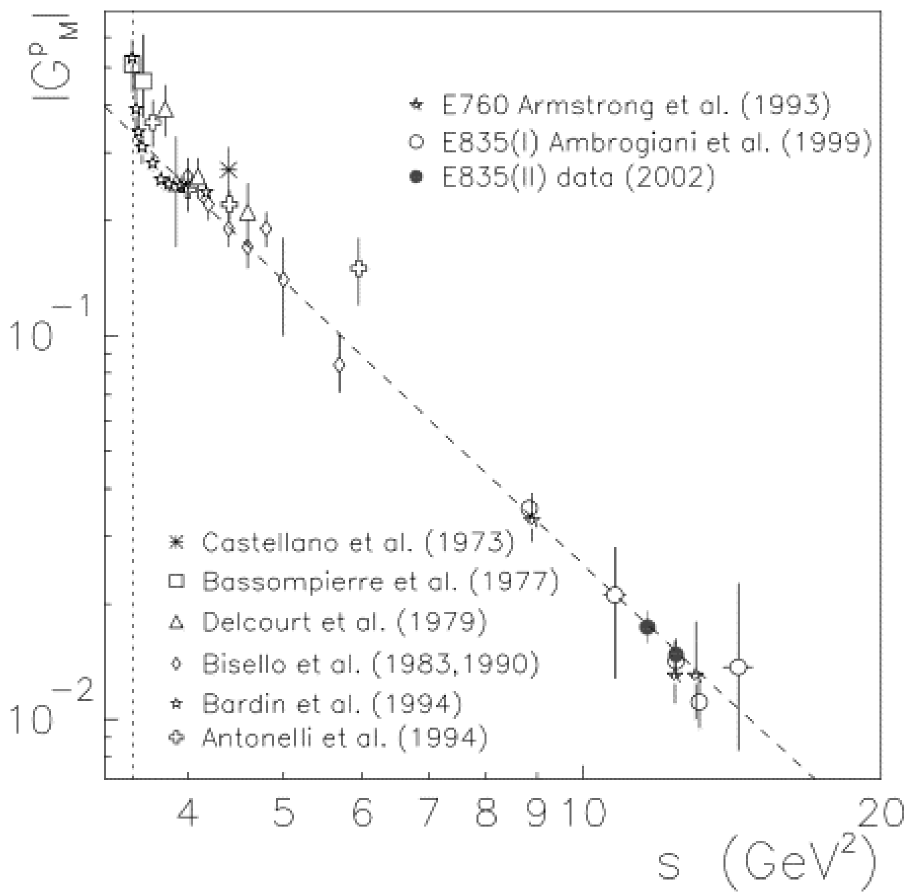

Figure 3: All existing magnetic form factor data of the proton in the time–like region obtained with the hypothesis $|G_M| = |G_E|$ versus $s = q^2$, as compiled in [36], the summary of the earlier data can be found in [44].

by pQCD. The PAX experiment would measure the relative phase ϕ_{EM} of the form factors from the SSA data with the transversely polarized proton target.

The modulus of G_E and G_M can be deduced from the angular distribution in an unpolarized measurement for $\bar{p}p \to e^+e^-$ as it can be carried out independently at PANDA as well as at PAX. However, the additional measurement of the transverse double spin asymmetry in $p^\uparrow \bar{p}^\uparrow \to \ell^+\ell^-$ that is feasible at PAX could further reduce the systematic uncertainties of the Rosenbluth separation. Furthermore, after the spin filtering the polarization of the proton target can be changed to the longitudinal direction, and the in–plane longitudinal–transverse double spin asymmetry would allow one [8] to measure the $\mathrm{Re}G_E^* G_M$, which would resolve the remaining $\phi_{EM} - (\pi - \phi_{EM})$ ambiguity from the transverse SSA data. This will put tight constraints on current models of the form factor.

1.4 Hard Scattering: Polarized and Unpolarized

From the point of view of the theory of elastic and exclusive two–body reactions, the energy range of HESR corresponds to the transition from soft mechanisms to hard scattering with the onset of the power laws for the s, t, u–dependence of the differential cross sections [13, 14] which have generally been successful so far (for the review and further references see [46]). There remains, though, an open and much debated issue of the so–called Landshoff independent scattering–mechanism [16] which gives the odd–charge symmetry contribution to the NN and $\bar{N}N$ amplitudes and may dominate at higher energies. The more recent realization of the importance of the so–called handbag contributions to the amplitudes of exclusive reactions made possible direct calculations of certain two–body annihilation cross sections and double–spin asymmetries in terms of the so–called Generalized Parton Distributions (GPD's) [47, 48, 49]. The PAX experiment at HESR is uniquely poised to address several new aspects of hard exclusive scattering physics:

- The particle identification in the forward spectrometer of PAX would allow the measurement of elastic $p\bar{p}$ scattering in the small to moderate large $|t|$ in the forward hemisphere and, more interestingly, the backward hemisphere at extremely large t not accessible in the $t - u$ symmetric pp scattering.

- The high energy behavior of exotic baryon number, $B = 2$, exchange in the u–channel is interesting by itself. Its measurements in the small to moderately large u region of backward elastic $\bar{p}p$ scattering will be used for the isolation of hard $p\bar{p}$ scattering contribution at large $|u|$.

- After the isolation of the hard–scattering regime the importance of the odd–charge symmetry Landshoff (odderon) mechanism can be tested from the onset of hard scattering regime in large–angle elastic $\bar{p}p$ scattering as compared to pp scattering.

- The relative importance of odd–charge vs. even–change symmetric mechanisms for the large transverse double spin asymmetry A_{TT} in polarized $p^{\uparrow}p^{\uparrow}$ as observed at Argonne ZGS and BNL AGS can be clarified by a measurement of A_{TT} in polarized $\bar{p}^{\uparrow}p^{\uparrow}$ elastic scattering at PAX and the comparison with the earlier data form $p^{\uparrow}p^{\uparrow}$ scattering.

- The future implementation of particle identification in the large angle spectrometer of PAX would allow an extension of measurements of elastic scattering and two–body annihilation $\bar{p}p \to \gamma\gamma, \gamma\pi^0, \pi^+\pi^-, K^+K^-, \Lambda_c\Lambda_c, ...$ to large angles $\theta_{cm} \sim 90^o$.

The theoretical background behind the high–t possibilities of PAX can be summarized as follows:

The scaling power law s^{-N} for exclusive two–body hard scattering has been in the focus of high–energy scattering theory ever since the first suggestion in the early 70's of the constituent counting rules by Matveev et al. [13] and Brodsky & Farrar [14]. The subsequent hard pQCD approach to the derivation of the constituent counting rules has been developed in late 70's–early 80's and has become known as the Efremov–Radyushkin–Brodsky–Lepage (ERBL) evolution technique ([50, 51], see also Chernyak et al. [52], for the review of the status of the scaling laws see [46] and references therein). The scale for the onset of the genuine pQCD asymptotics can only be deduced from the experiment, on the theoretical side the new finding is the importance of the so–called handbag mechanism in the sub–asymptotic energy range [53, 54]. As argued by P. Kroll et al., the handbag mechanism prediction for the sub–asymptotic s–dependence of the large–angle elastic pp and $p\bar{p}$ cross–section [15] ,

$$\frac{d\sigma}{dt} \propto \frac{1}{s^2 t^8} \propto \frac{f(\theta)}{s^{10}} \tag{7}$$

is similar to that of the constituent quark counting rules of Brodsky et al. [14].

There remains, though, an open and hot issue of the so–called Landshoff independent scattering–mechanism [16], which predicts $d\sigma/dt \propto 1/t^8 \propto f_L(\theta)/s^8$ and, despite the Sudakov suppression, may dominate at very large s. According to Ralston and Pire [17] certain evidence for the relevance of the Landshoff mechanism in the HESR energy range comes from the experimentally observed oscillatory s–dependence of $R_1 = s^{10} d\sigma/dt$, shown in Fig. 4. Here the solid curve is the theoretical expectation [17] based on the interference of the Brodsky–Farrar and Landshoff mechanisms.

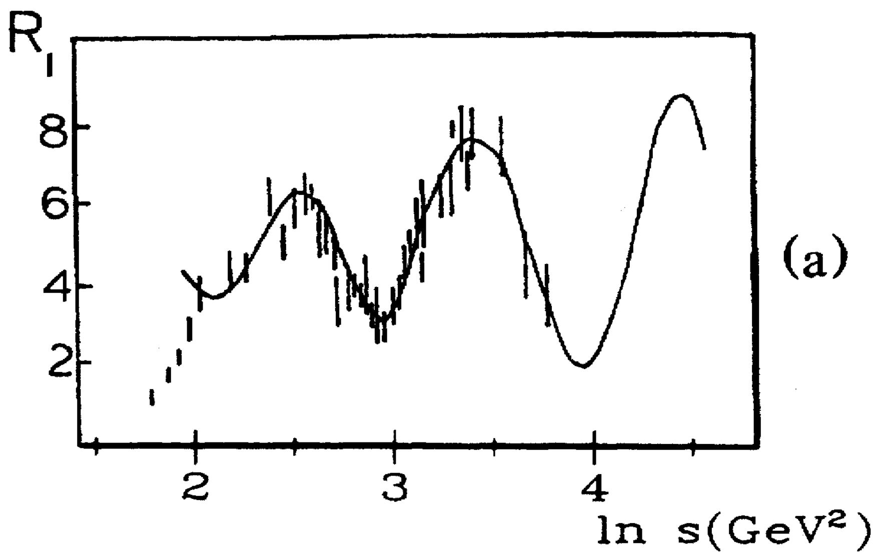

Figure 4: The energy dependence of $R_1 = s^{10} d\sigma_{pp}/dt|_{90^o}$ for the high energy pp elastic scattering at 90^o c.m. angle compared to the model calculation [17] from the interference of the Brodsky–Farrar and Landshoff mechanisms.

The principal point is that the Landshoff amplitude corresponds to the odd–charge conjugation (odderon) exchange and alters the sign from the pp to the $p\bar{p}$ case, while the Brodsky–Farrar and/or it's handbag counterpart would not. Consequently, the Ralston–Pire scenario for the oscillations predicts the inversion of the sign of oscillation in R_1 from the pp to the $p\bar{p}$ case. Because the first oscillation in Fig. 4 takes place at $s < 20$ GeV^2, the $\bar{p}p$ elastic scattering at HESR is ideally suited for testing the Ralston–Pire scenario and constraining the Landshoff amplitude.

Here we recall that very large double transverse asymmetries have been observed in hard proton–proton scattering ([55] and references therein). The HESR data with polarized antiprotons at PAX will complement the AGS–ZGS data in a comparable energy range. The helicity properties of different hard scattering mechanisms have been studied by Ramsey and Sivers [18]. These authors tried to extract the normalization of the Landshoff amplitude from the combined analysis of pp and $p\bar{p}$ elastic scattering and argued it must be small to induce the oscillations or contribute substantially to the double spin asymmetry A_{TT}. This leaves open the origin of oscillations in R_1 but leads to a conclusion that the double spin asymmetry A_{TT} in $p^\uparrow\bar{p}^\uparrow$ at PAX and $p^\uparrow p^\uparrow$ as observed at AGS–ZGS must be of comparable magnitude. The comparison of A_{TT} in the two reactions will also help to constrain the Landshoff amplitude.

In the comparison of observables for the pp and $\bar{p}p$ elastic scattering one would encounter manageable complications with the Pauli principle constraints in the identical particle pp scattering, by which the spin amplitudes for pp scattering have the t–u–(anti)symmetric form $M(\theta) \pm M(\pi - \theta) = M(t) \pm M(u)$ ([56] and references therein). Regarding the amplitude structure, the $\bar{p}p$ case is somewhat simpler and offers even more possibilities for the investigation of hard scattering. Indeed, for the hard scattering to be at work, in the general case one demands that both $|t|$ and $|u|$ are simultaneously large, $|t| \sim |u| \sim \frac{1}{2}(s - 4m_p^2)$. Here we notice an important distinction between the t–u asymmetric $\bar{p}p$ from the t–u symmetric identical particle pp elastic scattering. In the t–u symmetric case the accessible values of t are bound from above by $|t| \leq |t_{max}| = \frac{1}{2}(s - 4m_p^2)$. In the $p\bar{p}$ case the backward scattering corresponds to the strongly suppressed exotic baryon number two, $B = 2$, exchange in the u–channel (for a discussion of the suppression of exotic exchanges see [57, 58] and references therein). Consequently, the hard scattering mechanism may dominate way beyond $\theta_{\rm cm} = 90^o$ of $p\bar{p}$ elastic scattering. Because of the unambiguous p and $\bar{p}$ separation in the forward spectrometer, the PAX will for the first time explore the transition from soft exotic $B = 2$ exchange at $u \sim 0$ to the hard scattering at larger $|u|$: for 15 GeV stored $\bar{p}$'s the $p - \bar{p}$ separation is possible up to $|u| \leq 4$ GeV^2, while $|u| \leq 8$ GeV^2 is accessible at 22 GeV. Although still $|u| \ll s$, these values of $|u|$ are sufficiently large to suppress the u–channel exotic $B = 2$ exchange and allow an onset of hard mechanisms, which thus become accessible at values of $|t| = s - 4m_p^2 - |u|$ almost twice larger than in pp scattering at the same value of s. The investigation of the energy dependence of exotic $B = 2$ exchange in the small–u region is interesting by itself in order to better understand the related reactions like the πD backward elastic scattering.

Although not readily accessible with the present detector configuration, the annihilation reactions are extremely interesting because within the modern handbag diagram description they probe such fundamental QCD observables as the Generalized Parton Distributions (GPD's), introduced by Ji and Radyushkin [47, 48]. These GPD's generalize the conventional parton model description of Deep inelastic Scattering (DIS) to a broad class of exclusive and few–body reactions and describe off–forward parton distributions for polarized as well as unpolarized quarks; the Ferrara Manifesto, formulated at the recent Conference on the QCD Structure of the Nucleon (QCD–N'02), lists the determination of GPD's as the major physics goal of future experiments in the electroweak physics sector [49]. The QCD evolution of GPD's is a combination of the conventional QCD evolution for DIS parton densities and the ERBL evolution for the quark distribution amplitudes, they share with the DIS parton densities and the ERBL hard–scattering amplitudes the hard factorization theorems: the one and the same set of GPD's at an appropriate hard scale enters the calculation of amplitudes for a broad variety of exclusive reactions.

There has been much progress in calculating the electromagnetic form factors of the nucleon and of the hard Compton scattering amplitudes in terms of the off–forward extension of the conventional parton densities [53, 54, 59], Deeply Virtual Compton Scattering is being studied at all Electron Accelerators [60, 61] with the purpose to extract the specific GPD which would allow one to determine the fraction of proton's spin carried by the orbital angular momentum of partons (the Ji sum rule [47]).

More recently the technique of GPD's has been extended by P. Kroll and collaborators [62] to the differential cross sections and spin dependence of annihilation reactions. The theory has been remarkably successful in the simplest case of $B\bar{B} \to \gamma\gamma$ with two point–like photons (the inverse reactions $\gamma\gamma \to p\bar{p}$, $\Lambda\bar{\Lambda}$, and $\Sigma\bar{\Sigma}$ have been studied experimentally by the CLEO [63] and VENUS [64] collaborations). A steady progress is being made by the DESY–Regensburg–Wuppertal group in extending these techniques to the $p\bar{p} \to \gamma\pi^0$ with a non–point–like π^0 in the final state [65], a further generalization to the two–meson final states is expected in the near future. As far as the theory of spin dependence of hard scattering is concerned the theoretical predictions are robust for the longitudinal double spin asymmetries, and thus their experimental confirmation will be of great theoretical interest. Unfortunately, they will only be accessible experimentally if the spin of antiprotons will be rotated by Siberian Snakes. In addition, the technique of GPD's should allow one to relate the transverse asymmetries to the Generalized structure function h_1^q, see above, but such a relationship has yet to be worked out.

1.5 Polarized Antiproton–Proton Soft Scattering

1.5.1 Low–t Physics

For energies above the resonance region elastic scattering is dominated by small momentum transfers and therefore total elastic cross sections are basically sensitive to the small t region only.

Dispersion theory (DT) is based on a generally accepted hypothesis that scattering amplitudes are analytic in the whole Mandelstam plane up to singularities derived from unitarity and particle/bound state poles. This, in combination with unitarity and crossing symmetry, allows extracting of e.g. the real part of the forward elastic scattering amplitude from knowledge of the corresponding total cross sections. The major unknown in this context is the unphysical region: a left hand cut that starts at the two pion production threshold and extends up to the $\bar{N}N$ threshold, where one is bound to theoretical models for the discontinuity; the extrapolation to asymptotic energies is considered to be well understood [66] and does not effect the DT predictions in the HESR energy range.

Under certain assumptions, the real part of the forward scattering amplitude can be extracted from the elastic differential cross section measured in the Coulomb-nuclear interference (CNI) region ([67] and references therein). The most recent DT analysis [19] reproduces the gross features of the available data, still the experiment suggests more structure at low energies and there is a systematic departure of the theoretical prediction from the experiment in the region between 1 and 10 GeV/c. In particular the latest precise results from Fermilab E760 Collaboration [20] collected in the 3.7 to 6.2 GeV/c region are in strong disagreement with DT.

There are two explanations possible for this discrepancy. First one might doubt the theoretical understanding of the amplitude in the unphysical region. In this sense the DT analysis is a strong tool to explore the unphysical region. Since the discrepancy of the data to the result of the DT analysis occurs in a quite confined region, only a very pronounced structure in the unphysical region could be the origin. Such a structure can be an additional pole related to a $\bar{p}p$ bound state[1] discussed in Refs. [68, 69, 70, 71]. The appearance of a pole in the unphysical region might cause a turnover of the real part of the forward scattering amplitude to small values at momenta above 600 MeV/c [72, 73]. Indications of such states were seen recently at BES in the $J/\Psi \to \gamma \bar{p}p$ decay [74] and Belle [75, 76].

However, there is a second possible reason for the discrepancy of the DT result and the data, namely that not all assumptions in the analysis of CNI hold, the strongest one being a negligible spin dependence in the nuclear interference region [77]. A sizable spin dependence of the nuclear amplitude can well change the analysis used in Ref. [20], such a sensitivity to a possible spin dependence has been discussed earlier [78]. The quantities to be measured are $\Delta\sigma_T = \sigma(\uparrow\downarrow) - \sigma(\uparrow\uparrow)$ and $\Delta\sigma_L = \sigma(\rightleftarrows) - \sigma(\rightrightarrows)$, their knowledge will eliminate the model–dependent extraction of the real part of the $p\bar{p}$ scattering amplitude [79]. Please note, a sizable value of $\Delta\sigma_T$ or $\Delta\sigma_L$ at high energies is an interesting phenomenon in itself since it contradicts the generally believed picture that spin effects die out with increasing energy (see also previous section).

Thus, a measurement of $\Delta\sigma_{L/T}$ in the energy region accessible to HESR not only allows one to investigate spin effects of the $\bar{p}p$ interaction at reasonably high energies but also to pin down the scattering amplitude in the unphysical region to deepen our understanding of possible $\bar{p}p$ bound states. Especially a determination of $\Delta\sigma_T$ can be done in a straightforward way as outlined in the next section.

1.5.2 Total Cross Section Measurement

The unpolarized total cross section $\sigma_{0,\mathrm{tot}}$ has been measured at several laboratories over the complete HESR momentum range, however, the spin dependent total cross section is comprised of three parts [80]

$$\sigma_{\mathrm{tot}} = \sigma_{0,\mathrm{tot}} + \sigma_{1,\mathrm{tot}} \vec{P} \cdot \vec{Q} + \sigma_{2,\mathrm{tot}} (\vec{P} \cdot \hat{k})(\vec{Q} \cdot \hat{k}). \tag{8}$$

[1]Note, already the present analysis of Ref. [19] contains one pole.

where $\vec{P}, \vec{Q}$ are the beam and target polarizations and $\hat{k}$ the unit vector along the beam momentum. Note that the spin–dependent contributions $\sigma_{1,2}$ are completely unexplored over the full HESR energy range. Only one measurement at much higher energies from E704 at 200 GeV/c [81] has been reported using polarized antiprotons from parity–non–conserving $\bar{\Lambda}$–decays.

With the PAX experiment the transverse cross section difference $\Delta\sigma_T = -2\sigma_{1,\text{tot}}$ can be accessed by two methods:

(1) from the rate of polarization buildup for a transversely polarized target when only a single hyperfine state is used. The contribution from the electrons is known from theory and can be subtracted. However, the difference of the time constants for polarization buildup with hyperfine states 1 *or* 2 (cf. Fig. 6) injected into the target, would directly access $\Delta\sigma_T$, whereas the contribution from the electrons could be extracted from the average.

(2) from the difference in beam lifetime for a target polarization parallel or antiparallel to the beam. A sensitive beam–current transformer (BCT) can measure beam lifetimes of the antiproton beam after polarization and ramping to the desired energy. An accuracy at the 10^{-4} level has been achieved by the TRIC experiment at COSY using this method. Access to $\Delta\sigma_T$ by this technique is limited to beam momenta where losses are dominated by the nuclear cross section, e.g. above a few GeV/c – the precise limit will be determined by the acceptance of the HESR (cf. Sec. 6.1).

Both methods require knowledge of the total polarized target thickness exposed to the beam. With a calibrated hydrogen source fed into the storage cell, the target density can be determined to 2–3% as shown by the HERMES [82] and FILTEX [83] experiments.

In principle, $\Delta\sigma_L = -2(\sigma_{1,\text{tot}} + \sigma_{2,\text{tot}})$ can be measured by the same method, however, a Siberian snake would be needed in the ring to allow for a stable longitudinal polarization at the interaction point.

1.5.3 Proton–Antiproton Interaction

The main body of $\bar{N}N$ scattering data has been measured at LEAR (see [84] for a recent review) and comprises mainly cross section and analyzing power data, as well as a few data points on depolarization and polarization transfer. These data have been interpreted by phenomenological or meson–exchange potentials by exploiting the G–parity rule, linking the $\bar{N}N$ and the NN systems.

At the HESR the spin correlation parameters A_{NN}, A_{SS}, and A_{SL} can be accessed for the first time by PAX which would add genuine new information on the spin dependence of the interaction and help to pin down parameters of phenomenological $\bar{N}N$ models.

Besides, available data on the analyzing power from LEAR will be used for polarimetry to obtain information on the target and beam polarization, independent from the polarimeter foreseen for the polarized target (cf. Sec. 2.3).

2 Internal Polarized Gas Target and Antiproton Polarizer

2.1 Internal Polarized Gas Target

For the measurement of single–spin observables and for spin filtering of antiprotons and subsequent measurement of two spin–observables, a versatile polarized internal gas target for hydrogen and deuterium is required. Based on the experience at different experiments [85], a storage cell target, fed by an Atomic Beam Source (ABS) is proposed. The storage cell, a thin walled tube about 25 to 40 cm long is placed on–axis of the stored beam in the center of a low–β section in order to achieve the minimum tube diameter and thus the highest areal density d_t. For a round beam d_t scales with $\beta^{-3/2}$. Cooling of the cell down to about 80 K enhances the density by nearly a factor of 2, compared with a cell at room temperature.

ABS storage cell targets are well understood and reliable tools proven to run for periods of several months without service [86]. The areal densities achieved are of the order of a few $\times$ 10^{14} atoms/cm^2. A significant improvement by enhancing the source intensity, and by squeezing the diameter of the beam can be expected.

2.1.1 Storage Cell and Guide Field

As the highest possible d_t is mandatory, we propose to utilize a cold Al cell coated with Drifilm [87, 88] or Teflon, cooled to about 80 K. In order to monitor the target performance, a sampling polarimeter should be employed, enabling to check the setting of the ABS rf–transitions and the optimum quality of the cell walls.

For transverse target polarization a strong magnetic guide field B perpendicular to the $\bar{p}$ beam is required. B should be strong compared with B_c, the critical field of the target atoms ($B_c(H) = 50.7$ mT, $B_c(D) = 11.7$ mT). A high field is particularly important for the high anticipated densities in order to suppress efficiently spin–exchange depolarization. Thus a field of 0.3 T or higher is required leading to a significant deflection of the beam in particular at the lowest momenta of about 1.5 GeV/c. Here for minimum displacement a system of four correction dipoles is required.

2.1.2 Achievable Polarization

By employing two substates for both hydrogen and deuterium, the maximum possible polarization values can be obtained. If all rf–transitions are switched off, a purely electron polarized target is produced. By means of the above mentioned sampling polarimeter, the polarization of the target can be determined up to a precision of about 3 % [86].

2.2 Antiproton Polarizer

In 1992 an experiment at the Test Storage Ring at Heidelberg, Germany, showed that an initially unpolarized stored 23 MeV proton beam can be polarized by spin–dependent interaction with a polarized hydrogen gas target [83, 89, 90]. This *Spin–Filter* Experiment made use of the fact, that the total hadronic *pp* cross section is spin–dependent. In the presence of polarized protons of magnetic quantum number $m = \frac{1}{2}$ in the target, beam protons with $m = \frac{1}{2}$ are scattered less often, than those with $m = -\frac{1}{2}$, which eventually causes the stored beam to become partially polarized. The acquired polarization is parallel to the proton spin of the hydrogen gas target during the filtering process. The effective polarizing cross section was measured to be $\sigma_{\text{eff}} = 72.5$ mb. This experimental result cannot be explained by the total hadronic cross section of $\sigma_{\text{hadr}} = 122$ mb only.

Meyer reanalyzed the TSR experiment and identified three different mechanisms, that add up to almost exactly the measured result. One of these mechanisms is spin–transfer from the polarized electrons of the hydrogen gas target onto the circulating protons. Horowitz and Meyer derived the spin transfer cross section ($p + \vec{e} \rightarrow \vec{p} + e$) (using $c = \hbar = 1$) for a transversely polarized electron target [91, 92],

$$\sigma_{e_\perp} = -\frac{1}{2}\left[\frac{4\pi\alpha^2(1+\lambda_p)m_e}{p^2 m_p}\right] C_0^2 \left[\frac{\nu}{2\alpha}\right] \times \sin\left[\frac{2\alpha}{\nu}\ln(2pa_0)\right] \ , \tag{9}$$

where α is the fine–structure constant, $\lambda_p = (g-2)/2 = 1.793$ is the anomalous magnetic moment of the proton, m_e and m_p are the rest masses of electron and proton, p is the momentum in the CM system, $a_0 = 52900$ fm is the Bohr radius and $C_0^2 = 2\pi\eta/[exp(2\pi\eta) - 1]$ is the square of the Coulomb wave function at the origin. The Coulomb parameter η is given by $\eta = -z\alpha/\nu$ [2], z is the beam charge number and ν the relative velocity of particle and projectile in the laboratory system. In Fig. 5 the spin transfer cross section $\sigma_{e_\perp}$ of antiprotons scattered from transversely polarized electrons is plotted versus the kinetic energy T. It should be noted, that the longitudinal spin–transfer cross section $\sigma_{e_\parallel} = 2 \cdot \sigma_{e_\perp}$ [91] would yield higher polarization, but it is much more complicated to realize, because it requires a Siberian snake at HESR to have a longitudinal stable spin direction at the target position.

For almost a decade, physicists have been trying to produce reasonably intense beams of polarized antiprotons. Because antiprotons annihilate with matter, conventional methods like atomic beam sources, appropriate for the production of polarized protons and heavier ions do not work for antiprotons. Polarized antiprotons have been produced in a double scattering setup, but the intensities achieved this way are small. Furthermore this method does not allow to accumulate a reasonable amount in a storage ring, which would greatly improve the luminosity for reactions involving antiprotons. Polarization transfer in *ep* scattering proposed by Horowitz and Meyer offers a completely new method to achieve the aspired goal. For example, if one could produce a sufficiently dense target of free polarized electrons, then one would be able in principle to produce stored polarized antiprotons

[2] Note: For antiprotons a positive η parameter must be used. For protons η is negative.

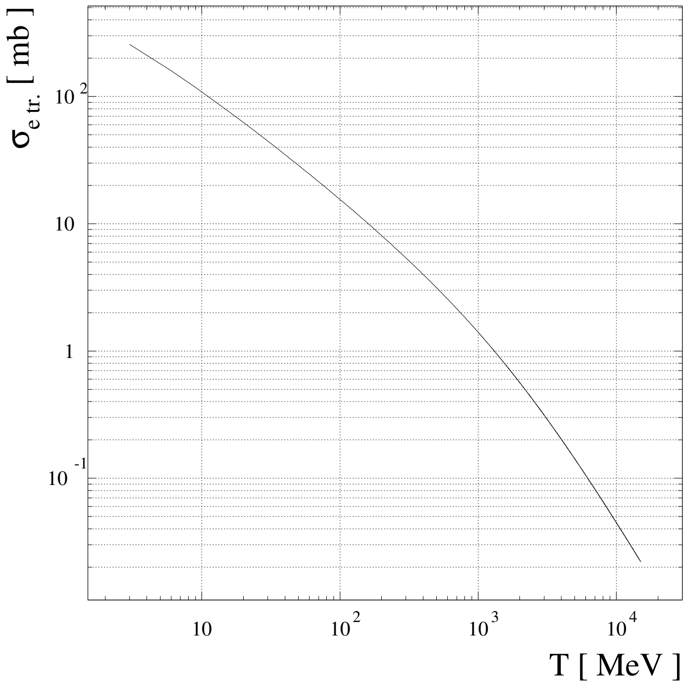

Figure 5: Spin transfer cross section $\sigma_{e_\perp}$ of antiprotons scattered from transversely polarized electrons ($p + \vec{e} \rightarrow \vec{p} + e$) as a function of the kinetic energy of the antiprotons.

almost without loss, because $\bar{p}e$ scattering angles are always small compared to the acceptance angle of any storage ring ($\psi_{\max} = m_e/m_p = 0.54$ mrad). More importantly, this new method needs no assumption about the spin–dependence in $\bar{p}p$ scattering. Even if it turns out, that the spin–dependence in $\bar{p}p$ scattering were small and therefore the earlier proposed method *Spin–Filtering using a Polarized Hydrogen Gas Target* [93, 94] becomes inefficient, a purely electron–polarized electron or gas target would still yield polarized antiprotons.

2.2.1 Polarized Electron–Target

It has been realized that, due to Coulomb repulsion and intensity limitations of polarized electron guns in DC–mode, the areal density of a free electron target is much lower than the one offered by a (neutral) storage cell gas target. A polarized hydrogen gas target is the best choice because the total hadronic cross section $\sigma_{\mathrm{tot}}(\bar{p}d)$ is about a factor of two larger than $\sigma_{\mathrm{tot}}(\bar{p}p)$ [95], which leads to a higher beam lifetime for a hydrogen target. The required purely electron–polarized hydrogen gas target can be obtained by injection of hyperfine states 1 and 2 together into a strong magnetic guide field (see Breit–Rabi diagram in Fig. 6). In a sufficiently strong magnetic field ($B \gg B_{\mathrm{c}} = 50.7$ mT) the nuclear

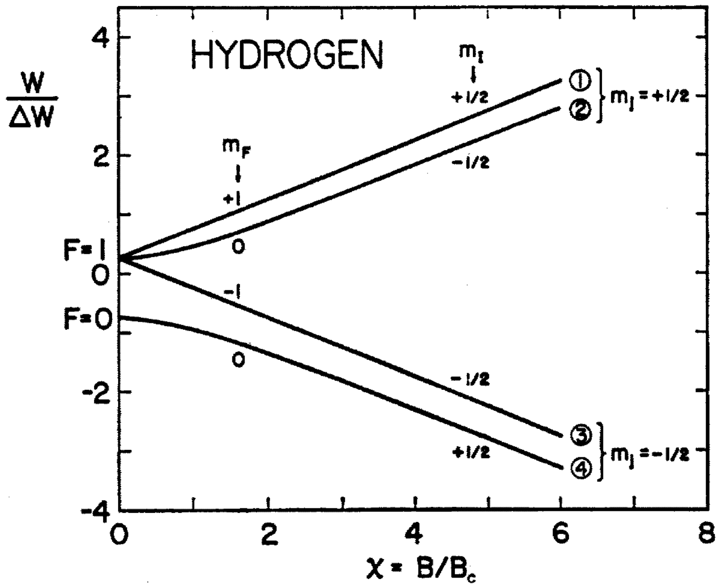

Figure 6: Breit–Rabi diagram of hydrogen atoms in units of $\Delta W = h \times 1420.4$ MHz [96]. The magnetic field is given in units of $\chi = B/B_c$. The critical field for the ground state of hydrogen is $B_c = 50.7$ mT.

polarization of states 1 and 2 adds to zero, whereas the electron polarization of these states equals 1. We propose to use a field of at least $B = 300$ mT, in which case the nuclear vector polarization of states 1 and 2 is $P_z = 7 \cdot 10^{-3}$, while the electron polarization is (ideally) $P_e = 0.99$. In reality, due to incomplete separation, wall depolarization and residual gas contributions, $P_e = 0.9$ can be expected.

2.2.2 Target Density

The antiproton beam will suffer a lateral displacement when passing through the cell region immersed in the transverse magnetic holding field. At momenta of 1 GeV/c, the antiproton beam is displaced by 7 mm in the middle of a 40 cm long cell immersed in a magnetic field of 0.3 T. In estimating the achievable target density we therefore took into account an elliptical cell with an horizontal axis of 21 mm and a vertical one of 5 mm. This constitutes a slightly reduced version of the cell which is currently used in the HERMES experiment in the HERA lepton ring (21 mm $\times$ 8.9 mm). The cell conductance at 100 K for a beam tube of dimensions 21 mm $\times$ 5 mm $\times$ 400 mm including a 10 mm diameter, 10 cm long, injection tube (like the ones used in HERMES) gives a value of 4.9 l/s. This value combined with an injected flux of polarized atoms of 5.5 $\times$ 10^{16} at/s (like the one which is currently obtained in HERMES) gives a total areal density of $2.1 \cdot 10^{14}$ cm^{-2} of atoms, and of polarized electrons at the same time.

2.2.3 Future Developments

Presently a source of the last generation implemented at the RHIC accelerator has declared measured fluxes of the order of 1.1×10^{17} atoms/s for an atomic polarized hydrogen beam. It is then reasonable to assume that densities of 5×10^{14} cm^{-2} should be reachable for the internal target. It is worthwhile to mention that different groups signing this Letter–of–Intent (Ferrara, Jülich, Erlangen) are presently involved in projects aiming at improving the intensity of the existing polarized sources, so that higher intensity sources might be available in a near future.

2.2.4 Polarization Buildup

The number N_0 of particles circulating in the ring decreases exponentially with time

$$N(t) = N_0 \cdot e^{-t/\tau_{\mathrm{b}}} \ , \tag{10}$$

where the time constant $\tau_{\mathrm{b}} = (f_{\mathrm{r}} \cdot d_t \cdot \sigma_{\mathrm{L}})^{-1}$ is the beam lifetime, which depends on the revolution frequency f_{r}, the target density d_t (atoms/cm^2) and the total loss cross section σ_{L}, which is discussed in Sec. 6.1 [97]. The stored beam current I is given by

$$I = N \cdot f_{\mathrm{r}} \ . \tag{11}$$

The polarizing mechanism (here $\sigma_{e_\perp}$) lifts e.g. antiprotons with magnetic quantum number $m = -\frac{1}{2}$ into state $m = +\frac{1}{2}$, therefore the occupation numbers of the two spin components in the beam change in time according to

$$N_{+\frac{1}{2}} = \frac{N_0}{2} \cdot \exp\left[-\frac{t}{\tau_{\mathrm{b}}}\right] \cdot \exp\left[+\frac{t}{\tau_1}\right] \tag{12}$$

$$N_{-\frac{1}{2}} = \frac{N_0}{2} \cdot \exp\left[-\frac{t}{\tau_{\mathrm{b}}}\right] \cdot \exp\left[-\frac{t}{\tau_1}\right] \ . \tag{13}$$

The time constant responsible for the polarization buildup is defined as

$$\tau_1 = (\sigma_{e_\perp} \cdot d_t \cdot f_{\mathrm{r}} \cdot Q)^{-1} \ , \tag{14}$$

where Q is the target polarization. The polarization of the stored beam after a time t is given by

$$P(t) = \frac{N_{+\frac{1}{2}} - N_{-\frac{1}{2}}}{N_{+\frac{1}{2}} + N_{-\frac{1}{2}}} = \tanh\left[\frac{t}{\tau_1}\right] \approx \sigma_{e_\perp} \cdot d_t \cdot f_{\mathrm{r}} \cdot Q \cdot t \ . \tag{15}$$

In Fig. 7, beam current and antiproton polarization are shown as a function of time for kinetic energies of $T = 0.5$ and 0.8 GeV. This estimate for the expected polarization buildup is based on the calculated beam lifetimes at HESR of about $\tau_{\mathrm{b}} = 10$ h in that energy range for an acceptance angle of HESR of $\psi_{\mathrm{acc}} = 10$ mrad, which is discussed in Sec. 6.1.

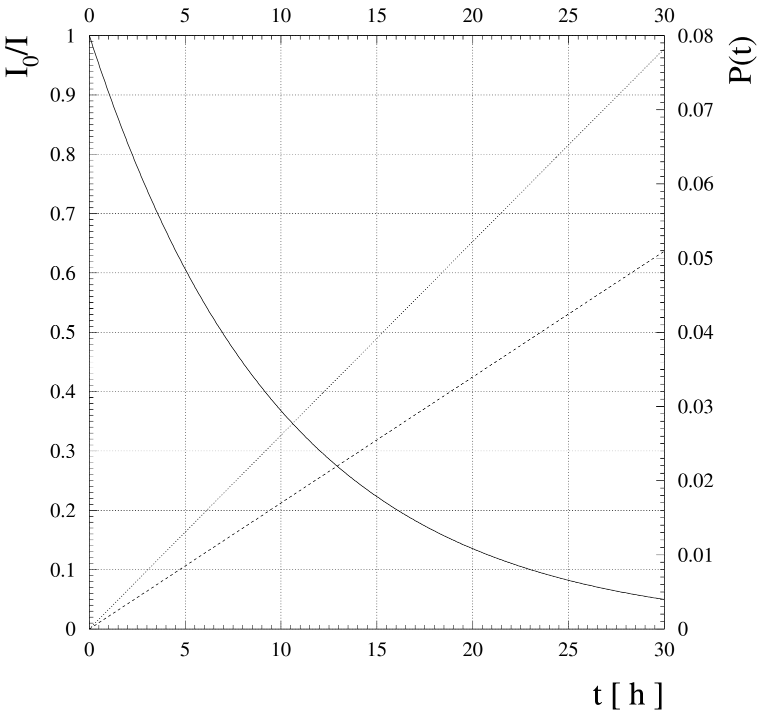

Figure 7: Beam current (solid line) and polarization buildup as a function of time in the antiproton beam, assuming an electron polarization of $P_e = 0.90$ and a target density of $d_t = 5 \times 10^{14}$ atoms/cm^2. The dashed line assumes a beam energy of $T = 800$ MeV, while the dotted line is for $T = 500$ MeV.

At a beam energy of for instance $T = 0.5$ GeV after a buildup time of 20 h (corresponding to two beam lifetimes), an antiproton polarization of $P = 0.052$ can be achieved. It should be noted that in this estimate the (unknown) effect from the hadronic interaction is not included. For *pp* scattering at $T = 500$ MeV the hadronic cross section responsible for the buildup, $\sigma_1 = -0.5 \cdot \Delta\sigma_{\mathrm{T}} = 3.6$ mbarn, is thus of the same order factor as the electromagnetic effect ($\sigma_{e_\perp}(500 \text{ MeV}) = 3.1$ mbarn). Since in the target one can choose freely the combination of electron and proton spins, the effects from hadronic and electromagnetic interaction can be added by injecting either hyperfine state 1 or 2 into the target. This would lead to the same polarization after two beam lifetimes, since the target density is also reduced by a factor two, but the antiproton beam intensity after filtering would be higher by about a factor e, compared to the situation depicted in Fig. 7.

2.3 Polarimetry

The beam and target polarization will be determined by the following scheme: First the target polarization using an unpolarized antiproton beam is established by either one of two methods:

(1) with reference to a suitable sampling polarimeter of the Breit–Rabi [98] or Lamb–shift [99] type, which spin–analyzes a small fraction of atomic hydrogen extracted from the target cell.

(2) elastic proton–antiproton scattering data at low energies (500–800 MeV) where analyzing power data from PS172 [100] are available. Scattering data of lower precision extend up to 2.5 GeV [101].

This allows one to calibrate a suitable detector asymmetry, derived from elastic scattering, in terms of an effective analyzing power. Since target and beam analyzing power in $\bar{p}p$ scattering are identical, the polarization of the beam can now be measured with an unpolarized target (e.g. by injecting unpolarized hydrogen gas into the cell). When subsequent fills of the HESR are made with different beam energies, it is straightforward to establish polarization standards at any energy within the HESR range by exploiting the fact, that the target polarization is constant with time – or monitored by the sampling polarimeter – and independent of energy [102].

3 Detector Concept

The PAX detector is a compact apparatus composed of two complementary parts. A forward detector of $\pm 8^o$ acceptance is designed to identify unambiguously the leading particles and precisely measure their momenta. A large acceptance central detector around the target measures angles and energies of the medium–energy electromagnetic particles in the exclusive channels like Drell–Yan. Reactions with two–body hadronic final states can be detected as well by identifying the leading hadron inside the forward detector and by measuring the scattering angles of the hadronic particles in the central detector. Both detectors can have a conventional structure.

At this preliminary stage, their designs are based on existing experiments which have been proven to work perfectly fine measuring final–state particles and energies similar to the ones of the PAX program.[3] The conventional design based on already existing detectors ensures the feasibility of a low–cost instrument suitable for the PAX physics program. The capability for operation at high rates is achieved by segmentation of the detectors and by equipping all channels with time-to-digital converters to allow rejection of out–of–time signals. The required π/e rejection factor, of the order of 10^{10} (corresponding to 10^5 for single track events), is achievable as demonstrated by previous measurements [105, 106]. Each of the detectors can be further optimized if the PAX experiment will be approved, i.e. the hadron identification at large scattering angles could be improved sizably adding an internally–reflecting ring–imaging Čerenkov [107] in the central detector.

[3] The forward detector design is based on HERMES [103], the large acceptance one on E835 [104]. Since these two experiments will terminate their physics program before the starting of PAX, it is possible that part of their equipment could be re–used in the present apparatus.

Both the central and the forward detector will be mounted on platforms which can move on rails in and out of the beam line. For simplicity, in the following we will refer only to Drell–Yan processes, the argument holds for J/Ψ decays and time–like electromagnetic form factors as well.

3.1 The Forward Spectrometer

To measure leading hadrons in inclusive, semi–inclusive and exclusive reactions an open spectrometer is the appropriate type of detector. The PAX spectrometer is a forward angle instrument of conventional design, consisting of a large–gap dipole magnet in combination with tracking systems. The scattering angles as well as the initial trajectory for the determination of the particle's momentum are measured by the front tracking system consisting of two sets of drift chambers (FC). The momentum measurement is completed by two sets of drift chambers behind the magnet (BC). A set of proportional chambers inside the dipole magnet (MC) improves the matching between the front and back tracking, helps to resolve multiple tracks and allows the low–momentum tracks which do not reach the backward section of the spectrometer to be detected. Particle identification is provided by a lead–glass calorimeter (CAL), a pre–shower detector (PS) and a transition radiation detector (TRD), designed to provide a hadron rejection factor greater than 10^4 (and $\lesssim 100$ at trigger level) to yield a very clean Drell–Yan data sample. A ring–imaging Čerenkov counter (RICH) is employed for the identification of charged hadrons (pions, kaons and protons). This provides flavor separation in the single–spin asymmetry investigations, as well as for the analysis of other semi–inclusive and exclusive channels. The electromagnetic calorimeter allows the reconstruction of neutral pions in the hadronic final state. The calorimeter and pre–shower detectors are included in the trigger along with a second hodoscope placed in front of the TRD and a third one before the front chambers.

The forward detector is divided into two identical halves placed above and below the beam line and is symmetric about a central plane containing shielding plates of the magnet field and supporting systems. Particles with scattering angles between $+(-)2^0$ and $+(-)8^0$ in the vertical and $\pm 8^0$ in the horizontal direction are accepted. A sketch of the forward spectrometer is shown in Fig. 8. A very similar scheme of the spectrometer has already been realized in the HERMES experiment [103].

The Magnet The spectrometer dipole magnet has field clamps in front as well as behind in order to reduce the fringe fields at the position of the drift chambers. A massive iron plate in the symmetry plane shields the antiproton beam as it passes through the magnet. The deflecting power is $\int Bdl = 1.3$ T $\cdot$ m whereas the fringe field at the position of the adjacent drift chambers does not exceed 0.1 T in order to give negligible deviations in the measured coordinates.

The Drift Chambers The drift chambers are of the conventional horizontal–drift type. They are assembled as modules consisting of three pairs of tracking planes with wires at

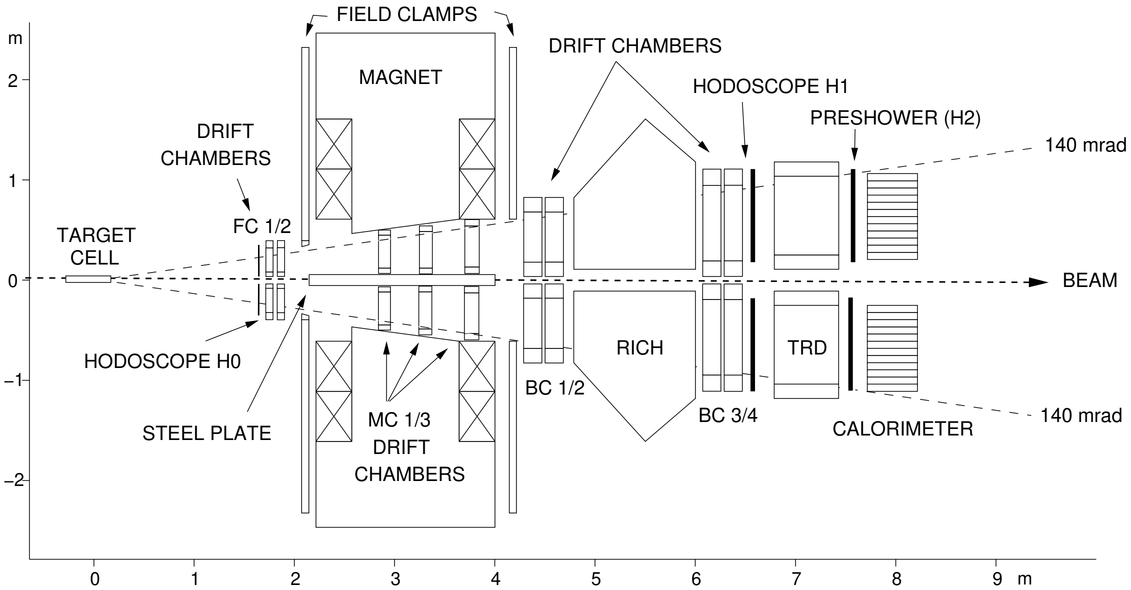

Figure 8: Sketch of the forward acceptance detector.

0^o and $\pm 30^o$ from the vertical. The wires of each adjacent plane are staggered in order to resolve left–right ambiguities. The DC readout system consists of amplifier/shaper/discriminator cards mounted on–board the drift chambers. The expected momentum resolution is $1-2$ % over the kinematic range of the experiment.

The Calorimeter The calorimeter consists of radiation–resistant F101 lead–glass blocks arranged in two walls of 42×10 blocks each above and below the beam. Each block is viewed from the rear by a photomultiplier tube (PMT). The blocks have an area of $9 \times 9\,\mathrm{cm}^2$ and a length of 50 cm (about 18 radiation lengths). The blocks are polished, wrapped with aluminized mylar foil and covered with a tedlar foil to provide light insulation. The expected energy resolution can be parameterized as $\sigma(E)/E[\%] = 5/\sqrt{(E[\mathrm{GeV}])} + 1.5$ which corresponds to 3–4 % at PAX energies. For an electron identification efficiency of 90 %, a hadron rejection factor of several hundreds can be achieved in combination with the pre–shower detector.

The Hodoscopes Three hodoscope planes are used for the trigger together with the calorimeter. A front trigger scintillator (H0) is placed directly upstream of the front drift chambers. It consists of a single sheet of standard plastic scintillator, 3.2 mm thick (0.7 % of a radiation length) read–out by two phototubes. A scintillator hodoscope in front of the TRD (H1) and a pre–shower counter (PS) in front of the calorimeter provide trigger signals and particle identification informations. Both counters are composed of vertical modules of fast scintillators with a large attenuation length (300–400 cm). The scintillation light is detected by photomultiplier tubes. A passive Pb radiator (2 radiation lengths) is placed in front of the PS hodoscope to initiate electromagnetic showers that deposit typically much more energy in the scintillator than minimal–ionizing particles.

The Transition Radiation Detector The detector consists of six modules above and below the beam. Each module contains a radiator and a proportional chamber. The radiator is made of a matrix of 20 μm diameter polypropylene/polyethylene fibers stitched in a low–density material and corresponds to an average of 267 dielectric layers. The proportional chambers have a conventional design with vertical wires. Xe/CH_4 can be used as the detector gas because of its efficient X–ray absorption. The signals from the wires are digitized by ADC's. Using a probability–based analysis of the size of the signals, a pion rejection factor greater than 10^3 for an electron efficiency of 90 % can be achieved.

The Ring–Imaging Čerenkov The RICH detector consists of two halves, above and below the beam pipe. Each half uses two radiators, a 5 cm thick 'wall' of silica aerogel tiles behind the entrance window and C_4F_{10} gas that fills the entire detector box. Charged particles with momenta above the corresponding thresholds produce Čerenkov photons in the radiators. These photons are reflected by aluminized carbon–fiber mirrors onto a detector plane that is located outside of the spectrometer acceptance. An ultra–relativistic particle ($\beta \sim 1$) will produce two concentric rings on the detector plane, a smaller gas ring and a larger aerogel ring. Each detector plane consists of a 70×30 matrix of small size (2 cm diameter) PMTs ordered on a hexagonal grid. The PMTs are read out digitally: as a result only the information is available if the PMT fired for a given event or not. The RICH provides particle identification for pions, kaons and protons in the momentum range from 2 to 15 GeV/c, with the aerogel radiator covering the low momentum region.

3.2 The Large Acceptance Spectrometer

To reveal the Drell–Yan processes, the PAX detector has to be able to measure electron pairs with large opening angle, in a wide kinematic range and with good angular and energy resolution. A clear identification of electrons is required to be able to separate scattered electrons of the Drell–Yan mechanism from the large π background. The forward spectrometer described above, with an acceptance of $\pm 8^0$, is therefore complemented with a large–acceptance non–magnetic apparatus, optimized to detect electromagnetic final states with two charged tracks of high invariant mass. This detector is placed in the free space between the target and the forward spectrometer, as sketched in Fig. 9. The inner detector is designed also to detect two–body hadron reactions by coplanarity and total momentum conservation requirements. Moreover it can measure the energy of gammas from radiative processes and π^0, η decays.

The very inner part of the detector is devoted to triggering and tracking of charged particles. It is composed of 2+2 layers of Scintillating Fibers (SCF) supported by caps shaped to optimize the acceptance and two straw chambers (SCH). A threshold Čerenkov counter (CER) provides trigger capability on electrons and positrons produced in Drell–Yan processes. Electron and photon energies and directions are measured by the electromagnetic

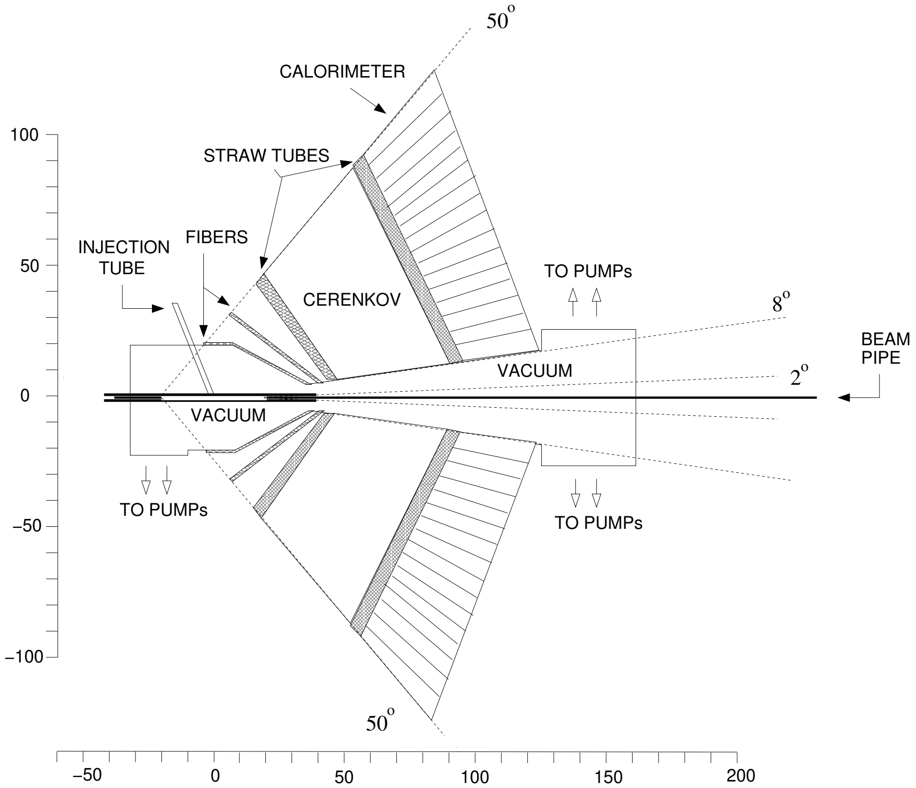

Figure 9: Sketch of the large acceptance detector.

calorimeter (CCAL). These devices have fast response and can be employed in the electromagnetic particles selection to get a π/e rejection factor $\lesssim$ 100 at trigger level and greater than 10^4 in the off-line analysis on a single track. The central detector is designed to give full acceptance between $\pm 8^0$ and $\pm 50^0$ for polar angles in the laboratory frame. It has a small not active region in the horizontal plane (corresponding to the polar $+(-)2^0$ blind region of the forward detector) where the supports of the cells and the coils of the target magnet are mounted. In the present design, there is no real limit for the maximum acceptable polar angle: the above $\pm 50^0$ value can be taken as conservative. The inner detector points toward the central part of the interaction region in a projective geometry. See for reference [104]. A conic shape empty space around the beam pipe allows the forward tracks to be detected in the forward spectrometer.

The Scintillating Fiber Detector This detector is made by 4 layers of fibers, supported by 2 coaxial caps at 20 and 25 cm from the center of the cell. The Scintillating Fibers type SCSF–3HF have a diameter of 0.835 mm and an average attenuation length of 5.5 m. They are wound internally and externally on support caps. Each support is made of acrylic and has a thickness of 3.5 mm, corresponding to 0.9 % total radiation length at normal incidence. The first cap may be made thinner if supported by the vacuum–air diaphragm. Each fiber is located in U–shaped grooves machined on the external and internal surface of the caps. On one end, the fibers are aluminized, to increase the light yield and reduce its dependence on position along the fiber. On the other end light is detected by solid state photosensitive devices as the Visible Light Photon Counters (VLPC) produced by Rockwell International, with high Quantum Efficiency in the visible region (70% at 550 nm and a gain better then 2×10^4). The VLPCs have to be kept at 6.5 K, to display the optimal performance. The cryogenic system that house the VLPC, the *VLPC cassette*, has been developed in Fermilab, as part of the D0 and E835 experiments (cf. [108]). Thank to the VLPC fast response this detector can be used in the first level trigger logic.

The Straw Chambers Two chambers are built of proportional drift tubes (aluminized mylar straws) to meet requirements of high granularity, good angular resolution and low mass, needed keep multiple scattering and photon conversion at a minimum. The thickness (at 90^0) is of the order of 0.11 % radiation length. Each chamber consists of two pairs of straw tubes layers, which are staggered to resolve left–right ambiguities. The chambers have a spider's web geometry and are mounted in front and behind the Čerenkov detector adjacent to the quadrants of its surface. The tubes have a diameter ranging between 0.5 and 1 cm depending on the distance from the cell. They are self–supporting between two grooved supports lying on the vertical and horizontal planes which allows gas to flow continuously.

The Čerenkov Detector A threshold gas Čerenkov counter is used in the trigger to select electrons out of a large background of hadrons. The required hadron rejection factor for triggered events, of the order of 10^3, is achieved with a π/e rejection factor of $\lesssim 100$ for the single charged particle. The counter occupies a 60 cm thick shell around the inner tracking detector and is divided into four identical quadrants composed by several gas cells. Čerenkov photons are reflected by aluminized carbon-fiber mirrors toward photomultipliers that are located outside of the spectrometer acceptance.

The Electromagnetic Calorimeter The central electromagnetic calorimeter (CCAL) is an matrix of 1300 Schott F2 lead–glass Čerenkov counters pointing toward the central part of the interaction region in a projective geometry. It measures energy and position of the electromagnetic showers. Each counter is contained in a light–tight stainless–steel container which reduces the active surface in the polar (azimuthal) direction by 2 % (0.5 %). The expected energy resolution can be parameterized as $\sigma(E)/E[\%] = 6/\sqrt{(E[\mathrm{GeV}])} + 1.4$ which corresponds to $3-4$ % at PAX energies. It is used in conjunction with the Čerenkov counter to provide the π/e rejection factor requested at the trigger level and in the offline analysis.

3.3 Interference with Target and Beam

The target design is described in details elsewhere (Sec. 2). The polarized gas atoms leave the target cell at the open ends and are differentially pumped by two stages along the beam. This minimizes the degradation of the vacuum and thus its effect on the stored beam. The transition from the cell to the beam pipe can be made smooth using perforated tubes, to avoid the generation of wake fields that could cause heating and increase the emittance of the beam. Given the extreme importance of the acceptance in the forward direction, the first pumping system at the cell position is located downstream. The vacuum region extends inside the conic–shaped internal space of the central detector and reaches the second pumping system placed just behind the CCAL and outside the acceptance of the forward detector (Fig. 9). Particles scattered into the central or forward detector exit the vacuum region through a 0.3 mm stainless steel foil (corresponding to 0.5 % of radiation length). A horizontal magnetic shielding substantially reduces the effect of the forward spectrometer magnet on the antiproton beam.

The Target Magnet In order to minimize the material inside the detector acceptance, the magnet is composed of two superconducting coils surrounding the target in the horizontal plane and providing a vertical field up to 0.3 T in the cell volume. The coils can be shaped or correcting coils can be added to improve the homogeneity of the field (if it is required to avoid depolarization effects from the beam current structure). The coils run inside a cooling tube where the liquid He is continuously flowing. The magnet is inside the vacuum region to provide thermal isolation. Four correcting dipoles are added to the beam line to compensate the effect of the PAX magnets on the antiproton orbit. For the case where longitudinal target polarization is requested, the transverse field applied in the polarization process will be ramped down. If only one hyperfine state is injected, the longitudinal holding field of some mT will be sufficient and can be provided by a couple of conventional Helmholtz coils. (When only one hyperfine state is injected in the target, spin–relaxation processes like spin–exchange collisions are practically absent and the condition for a strong holding field is consequently relaxed.)

3.4 Recoil Detector

A silicon recoil detector is needed for the low–t antiproton–proton elastic scattering program and will only be installed for these measurements, so that radiation damage will be a minor issue.

At very low momentum transfer ($|t| = 0.002 \dots 0.02$ GeV^2) the recoil protons are detected by silicon strip detectors close to 90° laboratory angle. At these angles (cf. Fig. 10a) the protons of interest have energies between 1 and 10 MeV and are stopped in a telescope comprised of a 65 μm thin surface barrier detector and a 1mm thick microstrip detector. Such a telescope [109] has already been successfully operated in a similar environment at the ANKE experiment at COSY/Jülich. In view of the comparably large cross section ($\mathrm{d}\sigma/\mathrm{d}t > 150$ mb/GeV^2) a precise measurement of the recoil *energy* is sufficient both to determine t and to cleanly identify elastically scattered protons as in the E760 experiment at FNAL [110].

Four of these detectors cover part ($\approx 50°$) of the four quadrants in the azimuthal angle ϕ as sketched in Fig. 10 (b). The acceptance is matched to the central part of the storage

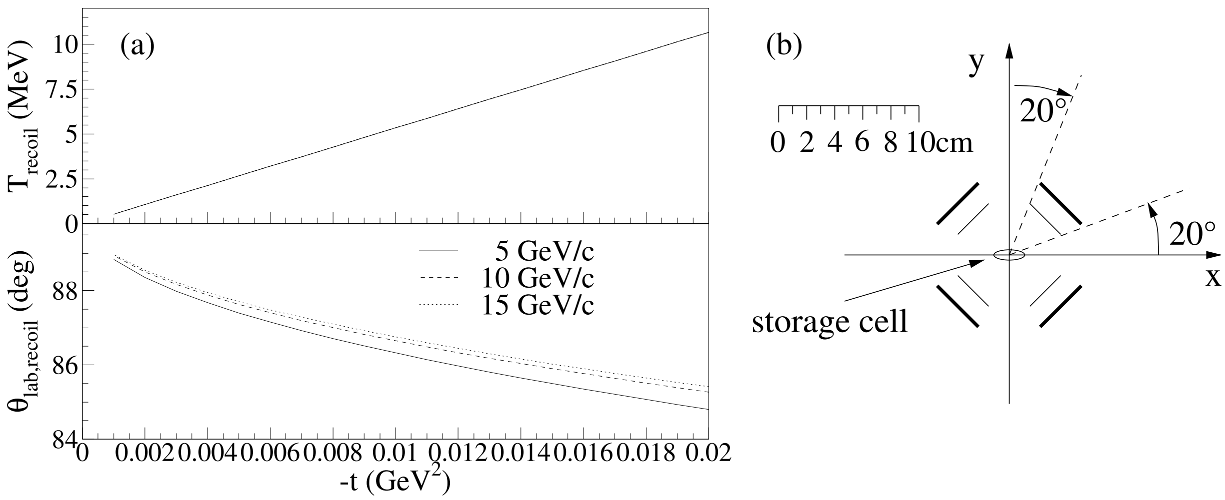

Figure 10: (a) Laboratory kinetic energy (top) and scattering angles (bottom) of the recoil proton for three different beam momenta. (b) Cross sectional view of the recoil detector.

cell. The cell walls can be made as thin as 5μm Teflon – as demonstrated by the PINTEX–experiment at IUCF [111] – and allow the detection of protons above 500 keV kinetic energy.

The spin–dependent cross section $\frac{\mathrm{d}\sigma}{\mathrm{d}t}$ for vertical beam polarization P_y and a transverse target polarization Q_x, or Q_y is given by

$$\begin{aligned}\frac{\mathrm{d}\sigma}{\mathrm{d}\Omega}(\vec{P},\vec{Q},\theta,\phi) = \frac{\mathrm{d}\sigma}{\mathrm{d}\Omega}\Big|_{\mathrm{unpol.}}(1 \quad &+ \quad [(P_y+Q_y)\cos\phi + Q_x\sin\phi]\,A_{\mathrm{N}} \\ &+ \quad P_yQ_y\left[A_{\mathrm{NN}}\cos^2\phi + A_{\mathrm{SS}}\sin^2\phi\right] \\ &+ \quad P_yQ_x\left[A_{\mathrm{SS}} - A_{\mathrm{NN}}\right]\sin\phi\cos\phi)\end{aligned} \tag{16}$$

which relates by integration over ϕ and change of variables to the differential cross section difference

$$\frac{\mathrm{d}\Delta\sigma_T}{\mathrm{d}t} = -\frac{\mathrm{d}\sigma}{\mathrm{d}t}\left(A_{\mathrm{NN}}(t) + A_{\mathrm{SS}}(t)\right) \tag{17}$$

with $\Delta\sigma_T = \sigma(\uparrow\downarrow) - \sigma(\uparrow\uparrow)$. With this experiment spin correlation parameter A_{NN}, A_{SS} as well as the analyzing power A_N of $\bar{p}p$ elastic scattering are accessible. However, the low recoil momenta prohibit the use of a strong target guide field, such that measurements must be taken after the polarization of the antiproton beam with a single pure hyperfine state and a weak (some mT) guide field to avoid strong bending of the recoils at very low t.

3.5 Trigger and Data Acquisition

For the different physics issues dedicated trigger schemes have to be used. For the detection of Drell–Yan electron pairs a coincidence comprising multiplicity information from the scintillating fibers, CCAL and segments of the Čerenkov counter in the central detector, and from the hodoscopes, pre-shower and CAL in the forward detector will be used. For single–spin asymmetries a single–prong trigger derived from the forward scintillator hodoscopes and the calorimeter can be used in a similar way as in the HERMES experiment [103]. For the low–t elastic antiproton–proton scattering the recoil–detector hodoscope provides self–triggering capability for low energy hadrons as demonstrated at ANKE [109].

High luminosity (above $10^{32}\,\mathrm{cm}^{-2}\mathrm{s}^{-1}$ in the case of unpolarized antiproton beam) and wide solid angle acceptance lead to high counting rates of the detectors. At such conditions the architecture of the trigger and data acquisition systems are essential in defining the capability of the setup to collect the data without large dead time losses.

The trigger system has to be flexible enough to cover different physics issues which demand different trigger selection criteria. It is planned to use a multilevel trigger comprised of a fast first level trigger and hardware and software processors at higher levels. The experience obtained in running of HERMES [103], ANKE [112] and other experiments [113] will be employed to a considerable extent. Due to the diversity of detectors used, sufficient capability for event-selection at the trigger level is available, like multiplicity information, energy loss and total energy measurements, particle identification, tracking and hit–map correlations.

To store the events during the processing at the low level trigger stages, pipelines and de-randomizing buffers will be used. The event builder will collect information from all the detector readout branches. The event builder protocol has still to be selected in view of fast developing network and computing technologies.

3.6 Physics Performance

The PAX experiment polarizes the antiproton beam by the spin filtering method and thus requires to fill the HESR up to the space–charge limit. A single machine cycle will typically last longer than a day, so that sufficient time to accumulate antiprotons in the injector chain is available.

Assuming spin filtering for about two beam lifetimes will yield polarizations in excess of 5% (cf. Sec. 2.2.4) at the expense of a reduction of the beam intensity by one order of magnitude. The design of the HESR [114] will allow to store $N_{\bar{p}} = 5 \cdot 10^{11}$ antiprotons circulating with a revolution frequency $f_r \approx 6 \cdot 10^5$ Hz. Assuming a target thickness of $d_t = 5 \cdot 10^{14}$ $\mathrm{cm}^{-2}\mathrm{s}^{-1}$ we expect a luminosity of

$$L = \frac{1}{10} N_p \cdot f_r \cdot d_t = 1.5 \cdot 10^{31} \frac{1}{\mathrm{cm}^2\mathrm{s}} \tag{18}$$

at the beginning of the measurement. For observables requiring only a polarized target, the luminosity will be larger by about a factor of ten. The time–averaged luminosity will be lower by a factor of three owing to the beam lifetime during the measurement and the duty–cycle.

The experimental uncertainty for double–spin asymmetries depends on the number of observed events N as well as the degree of polarization of the beam $|\vec{P}| \gtrsim 0.05$ and

		$\int_4^6 (d\sigma/dM^2)dM^2$	$\int_6^{16} (d\sigma/dM^2)dM^2$
	σ	1.1×10^{-6} GeV^{-2}	3.8×10^{-7} GeV^{-2}
$s = 30$ GeV^2	$\dot{N}$	186 events/day	65 events/day
	$\delta_{A_{TT}}$	10.4 %	17.6 %
	$\bar{x}$	$\simeq 0.40$	$\simeq 0.49$
	σ	1.9×10^{-6} GeV^{-2}	9.6×10^{-7} GeV^{-2}
$s = 45$ GeV^2	$\dot{N}$	323 events/day	161 events/day
	$\delta_{A_{TT}}$	7.9 %	11.2 %
	$\bar{x}$	$\simeq 0.33$	$\simeq 0.41$

Table 1: Integrated Drell–Yan cross sections, number of events per day, estimated error of A_{TT} and average value of x in the integrated region, for two values of s and two integration regions. The extremes of integration are expressed in GeV^2. The luminosity is taken to be 1.5×10^{31} cm $^{-2}$ s^{-1}. A duty cycle factor of 1/3 has been taken into account. The estimated errors come from the formula $\delta = \frac{1}{|\vec{P}||\vec{Q}|\sqrt{N}}$, assuming a polarization of the beam $|\vec{P}|$ of order 5%, a polarization of the target $|\vec{Q}|$ of order 90% and 240 days of data taking.

target $|\vec{Q}| \approx 0.90$. It is roughly given by $(|\vec{P}||\vec{Q}|\sqrt{N})^{-1} = 22/\sqrt{N}$. Note, that any beam polarization acquired in addition through the nuclear component of the target will reduce experimental uncertainties linearly.

For the estimate of count rates we will focus on the Drell–Yan process, the reaction with the highest demand on luminosity. Other reaction channels of interest, have larger cross–sections, or – like single–spin asymmetries – may use the unpolarized antiproton beam, where time averaged luminosities will be higher by a factor of 20.

In Tab. 1 the cross section σ for the Drell–Yan process, integrated over different $|Q^2| = M^2$–ranges are given as well as the expected count rates $\dot{N}$ and the precision $\sigma_{A_{TT}}$ for A_{TT} within 240 days of data taking. The definitive confirmation of the theoretical predictions of large A_{TT} in the 30–40 per cent range is possible already with 14.5 GeV antiprotons. The overall acceptance of the detector, neglected in these calculations, is around 70%. If antiprotons with an energy of 22.5 GeV are available, it is possible to measure h_1 at lower values of Bjorken x. Moreover the precision of the experiment improves.

These numbers entail only the non–resonant contribution to the Drell–Yan process, however, the J/Ψ will enhance the number of events in the $M^2 = 6$–16 GeV^2 range considerably.

For the program for low-t proton–antiproton elastic scattering, the recoil–detectors, with a typical area of 5×4 cm^2 each, will be mounted with the angular acceptance matched to the center of the storage cell. Count rates of 6×10^6/week per t–bin of 0.0005 GeV^2 width are expected to be achieved with a polarized antiproton beam of 5% polarization. Assuming a target polarizations of 90% spin correlation parameters can be measured to a precision of 0.01 within a week, so that this program can be finished within a few weeks.

Parts of the physics program with an unpolarized antiproton beam, as well as detector calibration and tuning, can be done parasitically to the PANDA experiment, provided beam energies and beam properties (low–β–function at the storage cell target, cf. next section) are suitable for PAX. In view of the PANDA target, being thicker by at least an order of magnitude than the PAX target, the disturbance of the beam due to PAX will be negligible.

4 Implementation

4.1 Experimental Area

4.1.1 Target IP and low–β Section

The achievable areal density of a storage cell target strongly depends on the vertical and horizontal dimensions of the beam at the target location. The beam dimension is proportional to the square root of the β–function, the target density is inversely proportional to the third power of the storage cell diameter, hence in total the target density is inversely proportional to $\beta^{3/2}$. The highest target density achieved in the HERMES experiment amounts to $2.1 \cdot 10^{14}$ atoms/cm^2 [86] In order to increase the available target density in a storage cell in the HESR, a low–beta section surrounding the target is required that provides $\beta = 1$ m. An acceptance angle of ψ_{acc} and a machine acceptance of $\epsilon_{\text{max}} = 100$ mm mrad is requested in order to get a beam life time of about 10 h at 0.8 GeV (see Fig 12). The distance from the IP to the next neighboring quadrupole is about 10 m. The ion–optical design of the experimental straight section has to be reconsidered. A very preliminary redesign of the experimental straight section shows the possibility to locate the PAX target section with the required β–function of 1 m at a distance of 35 m upstream or downstream of the PANDA IP.

4.1.2 Polarization Conservation in HESR

Acceleration and storage of polarized protons and antiproton beams in medium and high energy circular accelerator is complicated by numerous spin resonances. It is particularly difficult in the medium energy range ($T = 5$ to 10 GeV) since the necessary large orbit excursions make it very hard to install a full Siberian dipole snake [115] to correct all spin resonances. Full Siberian solenoid snakes need an excessively high integrated longitudinal field in this energy range. Individual manipulation of single spin resonances utilizing different techniques is needed [116]. In the HESR 27 Imperfection spin resonances can lead to beam depolarization ($\gamma G = 4, 5, 6, ..., 30$). The cooler solenoid acting as a partial snake and/or vertical correcting dipole can be utilized to preserve the polarization during spin resonance crossing [117]. For stored polarized beams a very accurate orbit correction is needed. With the existing HESR lattice, 54 intrinsic spin resonances are excited. If a super–periodicity of 12 in the arcs of the HESR can be achieved, 4 of theses spin resonances ($\gamma G = 0 + Q_y, 12 + Q_y, 24 - Q_y, 36 - Q_y$) remain very strong [118]. By exciting a coherent spin resonance excited with an AC dipole, polarization can be preserved during crossing strong intrinsic spin resonances [119]. For the additional weaker intrinsic spin resonances, generated by non–telescopic straight sections, a vertical tune jump system has to be installed [116, 120]. For stored beams a suitable tune setting has to be found to stay away from intrinsic spin resonances. To avoid coupling spin resonances, the phases space coupling introduced by the cooler solenoid has to be locally compensated.

4.1.3 Acceleration of the Polarized Antiproton Beam

The polarizing process by spin filtering has to be done in HESR at the lowest possible energy ($T = 0.8$ GeV or below). The measurements are performed in the full energy range of HESR. Therefore, acceleration of the polarized antiproton beam is required.

4.1.4 Floor Space

It is assumed that the experiment can move in and out of the beam position, and that there is a ’service position’ (out) where the experiment is fully outside of the machine area, separated by a 1.5 m shielding wall.

The electronics is located in an ’Electronic Trailer’ connected rigidly with the platform. Both systems can be moved together on rails. It is assumed that the whole space of about 300 m^2 in area is surrounded by an additional 2 m wide strip (walking, shielding wall etc.) resulting in a total floor hall space of about 450 m^2 (Tab. 2).

Experiment on a movable platform	$12 \times 7\ \mathrm{m}^2$
Electronic Trailer movable with platform	$12 \times 4\ \mathrm{m}^2$
Total space for in–beam position and service position	450 m^2

Table 2: Floor space requirements for PAX.

Concerning the required height of the experimental hall, we assume a beam 3 m above the platform and 5 m above the floor. The upper edge of the detector frames is assumed at 7.5 m above floor, resulting in a maximum height of the crane hook of 10.5 m above the floor. With 1.5 m for the crane structure itself, an inner hall volume of about 5,400 m^3 is estimated (Tab. 3).

In addition laboratory space and a control room attached to the experimental hall are required.

Height of the experimental hall	12 m
Crane hook	10.5 m above floor
Assumed beam height	5 m above floor
Volume of the hall	$450\ \mathrm{m}^2 \times 12\,\mathrm{m} = 5400\ \mathrm{m}^3$

Table 3: Requirements of the experimental hall for PAX.

4.2 Radiation Environment

The PAX experiment will operate with long beam lifetimes and thus slow antiproton consumption. Requirements for radiation safety at the target location will not be enhanced with respect to other areas along the HESR.

4.3 Cost Estimates

The figures listed in Tab. 4 are based on the 1993 figures of the HERMES TDR [121], increased by 30% for inflation.

1. Forward Spectrometer: HERMES Spectrometer magnet plus detectors. The magnet might be available after 2007.
2. Target: Here parts of the HERMES and/or ANKE targets can be recuperated, which might result in a reduction of the order of 20%.
3. Backward detector: Here the structure of the E835 detector has been assumed, calculated using HERMES figures (Cherenkov and Calorimeter) and the price of the HERMES recoil detector for the tracking part.
4. Infrastructure: These costs are also based on HERMES figures for Platform and support structures, cabling, cooling water lines, gas supply lines and a gas house, cold gases supply lines, electronic trailer with air conditioning etc.

Forward spectrometer a la HERMES	12.0 MEU
Large acceptance detector	2.6 MEU
Target	1.8 MEU
Infrastructure (cabling, cooling, platform, shielding)	3.0 MEU
Total	19.4 MEU

Table 4: Cost estimate for the PAX experiment.

4.4 Organization and Responsibilities

- **Target**
  Ferrara, Erlangen, Jülich.
  - Target Magnet
    Ferrara, Gatchina.
- **Forward Spectrometer**
  - Magnet
    Gatchina.
  - Drift Chambers
    Gatchina.
  - Electromagnetic Calorimeter
    Erlangen, Frascati
  - Particle Identification
    * Transition Radiation Detector
      Dubna.
    * Ring Cherenkov
      Dubna.
- **Large Acceptance Spectrometer**
  - Scintillating Fibers Detector
    Ferrara, Frascati, Bonn.
  - Straw Tubes
    Jülich.
  - Gas Cherenkov
    Gent.
  - Recoil Detector
    Jülich.
- **Data Acquisition and Trigger**
  Protvino, Gatchina.
- **Computing**
  Ferrara, Protvino, Dubna, Gatchina.

5 Time Schedule

The schematic time schedule presented here in Fig. 11 is divided into the different major setup components of the PAX experiment: target, forward spectrometer and large acceptance spectrometer.

As mentioned in the text, different groups signing this Letter–of-Intent are already involved in the development of an high intensity Atomic Beam Source, in particular making use of superconducting magnets. The related achievements will become useful also for the design of the superconducting magnet which will produce the transverse holding field for the target.

The presented time schedule is taking into account the possibility of making use of part of the HERMES spectrometer at HERA. The timing for HERA foresees running until the middle of 2007. In the meantime simulation studies will be performed to optimize the HERMES spectrometer for the PAX geometry.

The simulation and design of the Large Acceptance Spectrometer will proceed in a parallel and complementary way.

6 Appendix

6.1 Beam Lifetimes in HESR

The lifetime τ_b of the stored beam is given by

$$\tau_\mathrm{b} = \frac{1}{(\Delta\sigma_C + \sigma_0) \cdot d_t \cdot f} \,, \tag{19}$$

where $\Delta\sigma_C$ is the Coulomb–loss cross section and σ_0 corresponds to the total cross section for hadronic interaction, d_t is the density of both target and residual gas in the ring and f the revolution frequency of the beam. The electron cooling prevents particles with small scattering angles from being lost by reducing the emittance growth of the beam. Thus those particles are lost that undergo single Coulomb scattering at angles larger than the acceptance angle ψ_acc of the storage ring. The Coulomb–loss cross section $\Delta\sigma_C$ is obtained from integration over the Rutherford cross section

$$\Delta\sigma_C = \int_{\theta_\mathrm{min}}^{\theta_\mathrm{max}} \left(\frac{\mathrm{d}\sigma}{\mathrm{d}\Omega}\right)_\mathrm{Ruth.} \mathrm{d}\Omega \,. \tag{20}$$

The lower integration limit, the minimum loss angle θ_min is equal to the acceptance angle ψ_acc of the storage ring and the maximum loss angle equals 180° in the CM system. In the laboratory system integration yields for an antiproton beam of velocity v

$$\Delta\sigma_C = \frac{e^4}{2\pi\epsilon_0 m_\mathrm{p}^2 v^4} \left(\frac{1}{2\psi_\mathrm{acc}^2} - \frac{1}{2}\right) \,. \tag{21}$$

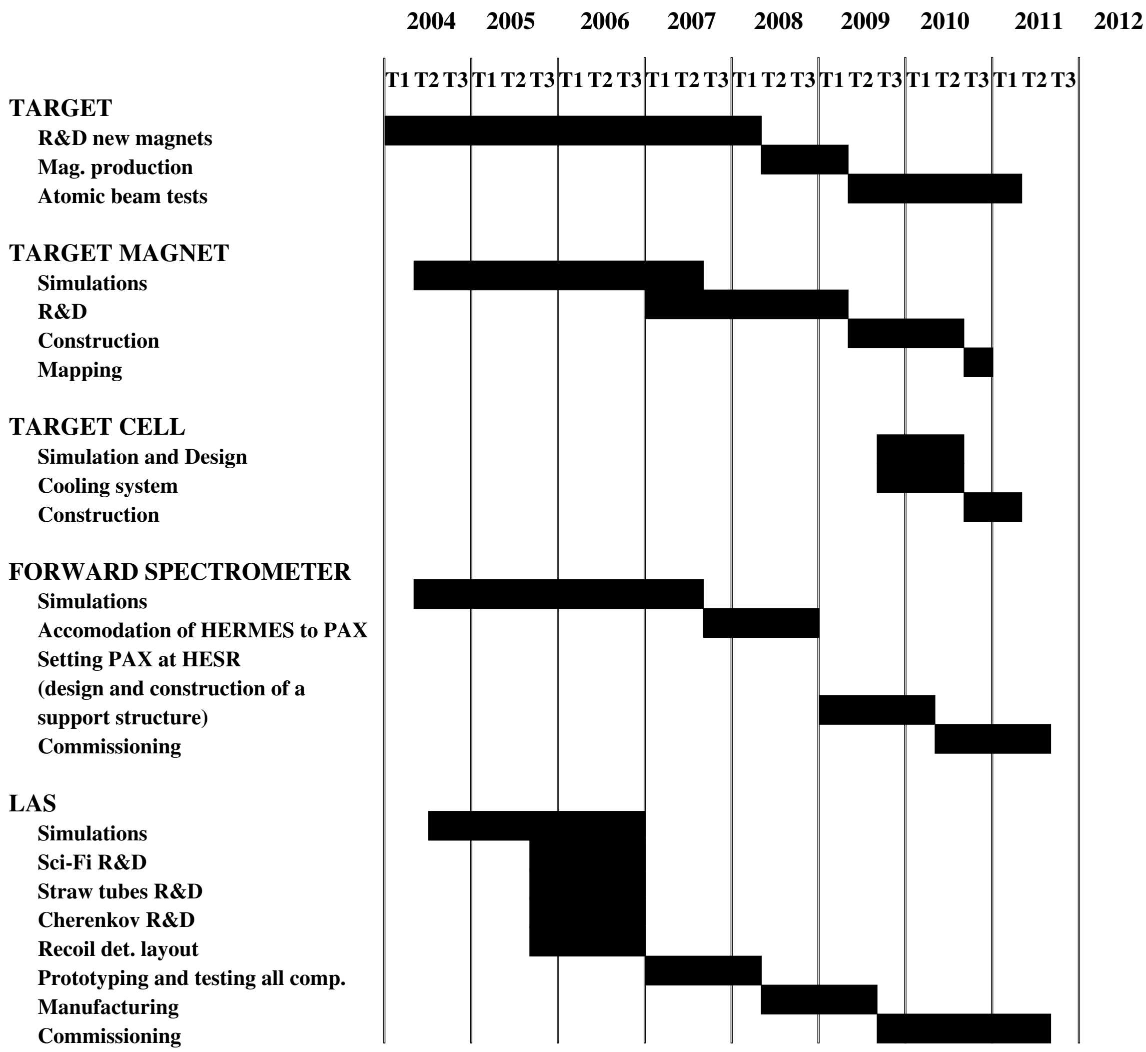

Figure 11: Time Schedule for the PAX experiment.

Together with the total hadronic cross section $\sigma_0 = \sigma_{\rm tot}(\bar{p}p)$ [95] evaluation of eq. (19) yields the beam lifetime as function of beam kinetic energy, depicted in Fig. 12, where the energy dependent orbit frequency f was determined for a HESR circumference of 444 m, and a target density of $d_t = 5 \times 10^{14}$ cm^{-2} is assumed.

Thus, in order to polarize the antiproton beam in HESR, an acceptance angle of at least $\psi_{\rm acc} = 10$ mrad is mandatory. The reference design of HESR with an acceptance of $\epsilon_{\rm max} \approx 20$ mm mrad yields with the required β–function of 1 m an acceptance angle of only $\psi_{\rm acc} = 4.5$ mrad.

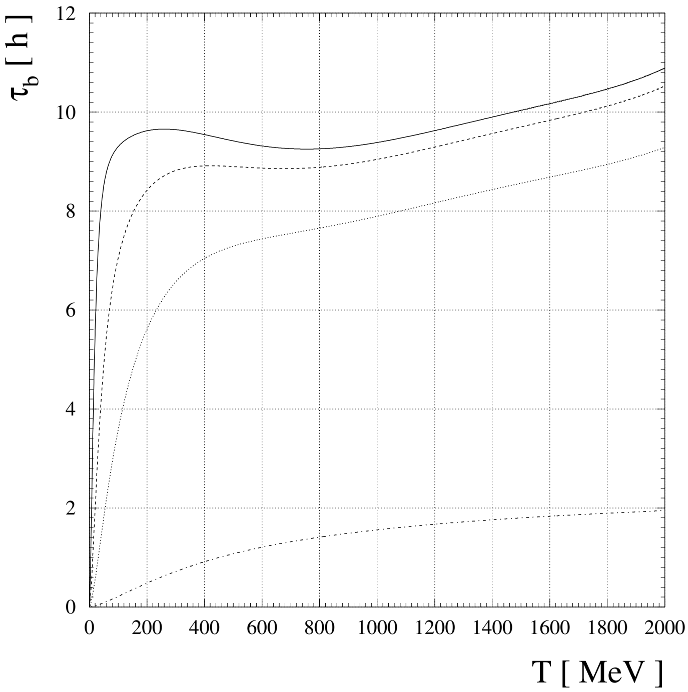

Figure 12: Beam lifetimes τ_b in HESR as a function of beam kinetic energy for different acceptance angles ψ_acc = 1, 5, 10 and 20 mrad and a target density of $d_t = 5 \times 10^{14}$ cm^{-2}.

References

[1] A comprehensive review paper on the transverse spin structure of the proton can be found in: V. Barone, A. Drago and P. Ratcliffe, Phys. Rep. **359** (2002) 1.

[2] M. Anselmino, V. Barone, A. Drago and N.N. Nikolaev, in preparation.

[3] K. Goeke, A. Metz and P. Schweitzer, private communication.

[4] HERMES Collaboration, A. Airapetian et al., Phys. Rev. Lett. **84** (2000) 4047; Phys. Rev. Lett. **90** (2003) 092002; Phys. Rev. **D64** (2001) 097101; K. Rith, Progress in Part. and Nucl. Phys. **49** (2002) 245.

[5] J.C. Collins, Phys. Lett. **b536** (2002) 43.

[6] D. Sivers, Phys. Rev. **D41** (1990) 83; Phys. Rev. **D43** (1991) 261.

[7] M. K. Jones et al., [Jefferson Lab Hall A Collaboration], Phys. Rev. Lett. **84** (2000) 1398. O. Gayou et al., [Jefferson Lab Hall A Collaboration], Phys. Rev. Lett. **88** (2002) 092301.

[8] A. Z. Dubnickova, S. Dubnicka, and M. P. Rekalo, Nuovo. Cim. **A 109** (1966) 241.

[9] S.J. Brodsky et al., hep–ph/0310277.

[10] For a discussion on the validity of continuing space–like form factors to the time–like region, see, B. V. Geshkenbein, B. L. Ioffe, and M. A. Shifman, Sov. J. Nucl. Phys. **20** (1975) 66 [Yad. Fiz. **20**, 128 (1974)].

[11] H.–W. Hammer, U.–G. Meißner and D. Drechsel, Phys. Lett. **B385** (1996) 343; H.–W. Hammer and U.–G. Meißner, arXiv: hep–ph/0312081.

[12] E. Tomasi–Gustafsson and M.P. Rekalo, Phys. Lett. **B504** (2001) 291; Nuovo Cim. **A109** (1996) 241.

[13] V. Matveev et al., Lett. Nouvo Cimento **7** (1972) 719.

[14] S. Brodsky and G. Farrar, Phys. Rev. Lett. **31** (1973) 1153 and Phys. Rev. **D11** (1973) 1309.

[15] M. Diehl, T. Feldmann, R. Jakob and P. Kroll, Phys. Lett. **B460** (1999) 204.

[16] P. Landshoff, Phys. Rev. **D10** (1974) 1024; P. Landshoff and D. Pritchard, Z. Phys. **C6** (1980) 69.

[17] J.P. Ralston and B. Pire, Phys. Rev. Lett. **61** (1988) 1823; ibid. **49** (1982) 1605; Phys. Lett. **B117** (1982) 233.

[18] G. P. Ramsey and D. W. Sivers, Phys. Rev. **D52** (1995) 116; Phys. Rev. **D47** (1993) 93; Phys. Rev. **D45** (1992) 79.

[19] P. Kroll and W. Schweiger, Nucl. Phys. **A503** (1989) 865.

[20] T.A. Amstrong et al., Phys. Lett. **B385** (1996) 479.

[21] J.C. Collins, Nucl. Phys. **B396** (1993) 161.

[22] K. Krueger et al., Phys. Lett. **B459** (1999) 412.

[23] D.L. Adams et al., Phys. Lett. **B264** (1991) 462; A. Bravar et al., Phys. Rev. Lett. **77** (1996) 2626.

[24] J. Adams et al., e–Print Archive: hep–ex/0310058.

[25] V. Barone, T. Calarco and A. Drago, Phys. Rev. **D56** (1997) 527.

[26] E. Anassontzis et al., Phys. Rev. **D38** (1988) 1377.

[27] P.L. McGaughey, J.M. Moss and J.C. Peng, Ann. Rev. Nucl. Part. Sci. **45** (1999) 217.

[28] N. Hammon, O. Teryaev and A. Schäfer, Phys. Lett. **B390** (1997) 409.

[29] D. Boer, P.J. Mulders and O. Teryaev, Phys. Rev. **D57** (1998) 3057.

[30] D. Boer and P.J. Mulders, Nucl. Phys. **B569** (2000) 505.

[31] D. Boer and J. Qiu, Phys. Rev. **D65** (2002) 034008.

[32] M. Anselmino, U. D'Alesio and F. Murgia, Phys. Rev. **D67** (2003) 074010.

[33] S.J. Brodsky, D.S. Hwang and I. Schmidt, Phys. Lett. **b530** (2002) 99.

[34] R. Baldini, S. Dubnicka, P. Gauzzi, S. Pacetti, E. Pasqualucci, and Y. Srivastava, Eur. Phys. J. **C11** (1999) 709; R. Baldini et al., *Proc. of the e^+e^- Physics at Intermediate Energies Conference* ed. Diego Bettoni, eConf **C010430**, T20 (2001) [hep–ph/0106006].

[35] See also R. Calabrese, in *Proc. of the e^+e^- Physics at Intermediate Energies Conference* ed. Diego Bettoni, eConf **C010430**, W07 (2001); H. W. Hammer, *ibid.*, W08 (2001) [arXiv:hep–ph/0105337]; Carl E. Carlson, *ibid.*, W09 (2001) [arXiv:hep–ph/0106290]; M. Karliner, *ibid.*, W10 (2001) [arXiv:hep–ph/0108106].

[36] M. Andreotti et al., Phys. Lett. **B559**, (2003) 20.

[37] A. Kaidalov, L. Kondratyuk and D. Tchekin, Phys. Atom. Nucl. **63** (2000) 1395.

[38] S. Rock, *Proc. of the e^+e^- Physics at Intermediate Energies Conference* ed. Diego Bettoni, eConf **C010430**, W14 (2001) [hep–ex/0106084].

[39] A. V. Belitsky, X. Ji, and F. Yuan, Phys. Rev. Lett. **91** (2003) 092003.

[40] J. P. Ralston and P. Jain, hep–ph/0302043; J. P. Ralston, P. Jain, and R. V. Buniy, AIP Conf. Proc. **549** (2000) 302 [hep–ph/0206074].

[41] G. A. Miller and M. R. Frank, Phys. Rev. **c65** (2002) 065205; M. R. Frank, B. K. Jennings, and G. A. Miller, Phys. Rev. **C54** (1996) 920.

[42] S. J. Brodsky, J. R. Hiller, D. S. Hwang, and V. A. Karmanov, e–Print Archive: hep–ph/0311218.

[43] F. Iachello, A. D. Jackson, and A. Lande, Phys. Lett. **B43** (1973) 191.

[44] M. Ambrogiani et al., Phys. Rev. **D60** (1999) 032002.

[45] T.A.Armstrong et al., Phys. Rev. Lett. **70** (1992) 1212.

[46] S. J. Brodsky, in Exclusive Processes at High Momentum Transfer, Workshop Proceedings, May 15–18, 2002. Jefferson Lab, Newport News, Virginia, editors A. Radyushkin and P. Stoler, World Scientific, pp. 1–33; S. J. Brodsky and G.P. Lepage, in Advanced Series on Directions in High Energy Physics, v. 5 : Perturbative Quantum Chromodynamics, editor A.H. Mueller, World Scientific (1989), pp. 93–240.

[47] X. D. Ji, Phys. Rev. Lett. **78** (1997) 610. X. D. Ji, Phys. Rev. **D55** (1997) 7114.

[48] A. V. Radyushkin, Phys. Lett. **B380** (1996) 417.

[49] THE QCD STRUCTURE OF THE NUCLEON (QCD–N'02). : Proceedings. Edited by E. De Sanctis, W.–D. Nowak, M. Contalbrigo, V. Muccifora. Amsterdam, Netherlands, North–Holland, 2002. Nucl. Phys. **A711** (2002).

[50] A. V. Efremov and A. V. Radyushkin, Phys. Lett. **B94** (1980) 245.

[51] G.P. Lepage and S.J. Brodsky, Phys. Rev. **D22** (1980) 2157.

[52] V. L. Chernyak, A. R. Zhitnitsky and V. G. Serbo, JETP Lett. **26** (1977) 594 [Pisma Zh. Eksp. Teor. Fiz. **26** (1977) 760]; V. L. Chernyak and A. R. Zhitnitsky, Phys. Rept. **112** (1984) 173.

[53] M. Diehl, T. Feldmann, R. Jakob and P. Kroll, Eur. Phys. J. **C8** (1999) 409.

[54] V. Barone, M. Genovese, N. N. Nikolaev, E. Predazzi and B. G. Zakharov, Z. Phys. **C58** (1993) 541.

[55] P. R. Cameron et al., Phys. Rev. **D32** (1985) 3070. G. R. Court et al., Phys. Rev. Lett. **57** (1986) 507. D. G. Crabb et al., Phys. Rev. Lett. **60** (1988) 2351. F. Z. Khiari et al., Phys. Rev. **D39** (1989) 45.

[56] C. Lechanoine–LeLuc and F. Lehar, Rev. Mod. Phys. **65** (1993) 47.

[57] C. Quigg, Nucl. Phys. **B34** (1971) 77.

[58] D. P. Roy, arXiv:hep–ph/0311207.

[59] A. Mukherjee, I. V. Musatov, H. C. Pauli and A. V. Radyushkin, Phys. Rev. **D67** (2003) 073014.

[60] L. Elouadrhiri, Nucl. Phys. **A711** (2002) 154. S. Stepanyan et al. [CLAS Collaboration], Phys. Rev. Lett. **87** (2001) 182002.

[61] V. A. Korotkov and W. D. Nowak, Eur. Phys. J. **C23** (2002) 455.

[62] M. Diehl, P. Kroll and C. Vogt, Eur. Phys. J. **C26** (2003) 567. M. Diehl, P. Kroll and C. Vogt, Phys. Lett. **B532** (2002) 99.

[63] M. Artuso et al. [CLEO Collaboration], Phys. Rev. **D50** (1994) 5484.

[64] H. Hamasaki et al. [VENUS Collaboration], Phys. Lett. **B407** (1997) 185.

[65] P. Kroll, private communication.

[66] A. Donnachie and P.V. Landshoff, Phys. Lett. **B296** (1992) 227; J. R. Cudell et al., Phys. Rev. **D65** (2002) 074024.

[67] R. Jakob and P. Kroll, Z. Phys. **A344** (1992) 87.

[68] L.N. Bogdanova, O.D. Dalkarov and I.S. Shapiro, Ann. Phys. **84** (1974) 261.

[69] I.S. Shapiro, Phys. Rept. **35** (1978) 129.

[70] G.C. Rossi and G. Veneziano, Phys. Rep. **63** (1980) 153.

[71] C.B. Dover, T. Gutsche and A. Faessler, Phys. Rev. **C43** (1991) 379.

[72] W. Grein, Nucl. Phys. **B131** (1977) 255.

[73] H. Kaseno et al., Phys. Lett. **B61** (1976) 203.

[74] Z. Bai et al., Phys. Rev. Lett. **91** (2003) 022001.

[75] K. Abe et al., Phys. Rev. Lett. **88** (2002) 181803.

[76] K. Abe et al., Phys. Rev. Lett. **89** (2002) 151802.

[77] C. Bourrely, J. Soffer and D. Wray, Nucl. Phys. **B77** (1974) 386.

[78] P. Jenni et al., Nucl. Phys. **B94** (1975) 1.

[79] R. Jakob and P. Kroll, Z. Phys. **A344** (1992) 87.

[80] J. Bystricky, F. Lehar, and P. Winternitz, J. Phys. **39** (1978) 1.

[81] D. P. Grosnick et al. [E581/704 Collaboration], Phys. Rev. **D55**, 1159 (1997).

[82] A. Gade "The HERMES unpolarized gas feed system, Version 4.0" HERMES internal report (2003).

[83] F. Rathmann et al., Phys. Rev. Lett. **71** (1993) 1379.

[84] E. Klempt, F. Bradamante, A. Martin, and J.–M. Richard, Phys. Rep. **368** (2002) 119.

[85] E. Steffens and W. Haeberli, Rep. Prog. Phys. **66** (2003) 1887.

[86] HERMES Collaboration, *The HERMES Polarized Target*, in preparation.

[87] G. E. Thomas et al., Nucl. Instrum. and Methods **A257** (1987) 32.

[88] D. R. Swenson and L.W. Anderson; Nucl. Instrum. Methods **B29** (1988) 627.

[89] K. Zapfe et al., Rev. Sci. Instrum. **66** (1995) 28.

[90] K. Zapfe et al., Nucl. Instrum. Methods **A368** (1996) 627.

[91] H.O. Meyer, Phys. Rev. **E50** (1994) 1485.

[92] C.J. Horowitz and H.O. Meyer, Phys. Rev. Lett. **72** (1994) 3981.

[93] P.L. Csonka, Nucl. Instrum. Methods **63** (1968) 247.

[94] H. Döbbeling et al., *Measurements of Spin–Dependence in $\bar{p}p$ Interaction at Low Momenta*, Proposal **CERN/PSSC/85–80** (1985) and Addendum (1986).

[95] K. Hagiwara et al., Phys. Rev. **D66** (2002) 010001.

[96] W. Haeberli, Ann. Rev. Nucl. Sci. **17** (1967) 373.

[97] R.E. Pollock et al., Nucl. Instrum. Methods **A330** (1993) 380.

[98] C. Baumgarten et al., Nucl. Instrum. Methods **A482** (2002) 606.

[99] R. Engels et al., Rev. Sci. Instr. **74** (2003) 4607.

[100] R.A. Kunne et al. Phys. Lett. **B206** (1988) 557; R.A. Kunne et al. Nucl. Phys. **B323** (1989) 1.

[101] M. G. Albrow et al., Nucl. Phys. **B37** (1972) 349.

[102] R.E. Pollock, Phys. Rev. **E55** (1997) 7606.

[103] K. Ackerstaff et al., (HERMES Collaboration) Nucl. Instrum. Methods **A417** (1998) 230.

[104] www.e835.to.infn.it/pub835.html.

[105] M. Ambrogiani et al., (E835 Collaboration) Phys. Rev. **D60** (1999) 032002.

[106] G. Bardin et al., (PS170 Collaboration), Nucl. Instrum. Methods **A259** (1987) 376.

[107] Aubert et al., (Babar Collaboration), Nucl. Instrum. Methods **A479** (2002) 1.

[108] M. Ambrogiani et al., IEE Trans. Nucl. Sci **44** (1997) 460.

[109] R. Schleichert et al., IEEE Trans. Nucl. Sci. **50** (2003) 301.

[110] T. A. Armstrong et al. Phys. Lett. **B385** (1996) 479.

[111] T. Rinckel et al., Nucl. Instrum. Methods **A439** (2000) 117.

[112] S. Barsov et al., Nucl. Instrum. Methods **A 462** (2001) 364.

[113] L. Afanasyev et al., Nucl. Instrum. Methods **A491** (2002) 376.

[114] L. Äystö et al., An International Accelerator Facility for Beams of Ions and Antiprotons, Conceptual Design Report, GSI (2001).

[115] Ya.S. Derbenev, A.M. Kondratenko, Part. Accel. **8** (1978) 115.

[116] F.Z. Khiari et al., Phys. Rev. **D39** (1989) 45.

[117] H. Huang et al., Phys. Rev. Lett. **73** (1994) 2982.

[118] A. Lehrach at al., Nucl. Instrum. Methods **A439** (2000) 26.

[119] M. Bai et al., Phys. Rev. Lett. **80** (1998) 4673.

[120] A. Lehrach at al., Acceleration of the Polarized Proton Beam in the Cooler Synchrotron COSY, Particle Accelerator Conference PAC 1999, New York.

[121] HERMES Collaboration: Techn. Design Report (1993) DESY-PRC 93/06.